Development of a Novel Pixelated Time Projection Chamber Detector: Q-Pix

Dissertation by

Kevin Keefe
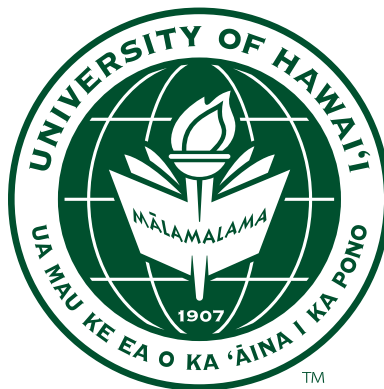
KE KULANUI O HAWAI'I MA MĀNOA

Mānoa, Hawai'i

2023

Dissertation Committee:

Kurtis Nishimura

Chairpersons

Jason Kumar, John Learned, Scott Rowland, Peter Sadowski, Gary Varner

Kevin Keefe
ORCID: 0000-0000

ACKNOWLEDGEMENTS

ABSTRACT

The Standard Model (SM) of physics has proven annoyingly successful in past decades, despite several measurements which hint at its incomplete description of nature. The hunt for New Physics (NP) continues at higher energies ($>> 1GeV$) with larger detectors ($\approx 10kT$). One such future detector is The Deep Underground Neutrino (DUNE) detector. DUNE (as any beam detector) is a combination of two detectors, a near-detector (ND) and a far-detector (FD) for long-baseline neutrino oscillation measurements. The DUNE FD will be a large scale ($\approx 40kiloton$) Liquid Argon Time Projection Chabmer (LArTPC). This 40-kT scale detector requires high precision in both timing ($<< \mu s$) and spatial resolutions ($\approx 1mm$) for vertex reconstruction of interesting neutrino events.

This dissertation discusses recent progress and characterizations of a novel implementation of new a pixelated LArTPC readout technology. This novel readout is based on a charge-integrate-reset circuit at the pixel level: Q-Pix. We present the basic pixel level readout circuit and the implications such an implementation has when applied at kiloton LArTPC scales. Further, we demonstrate results from the first-prototype implementation based on the Q-Pix readout which was designed with solely over-the-counter electronics. One problem of any pixelated readout is the the ability to handle a large number of unique data channels, which in the DUNE-FD is $\approx 10^8$. To address the scaling problem we developed and tested a modular digital back-end prototype as a proof of concept. In this dissertation, we discuss nominal system requirements to achieve DUNE-FD APA scale for radiogenic background sensitivity, as well as pixel-level calibration techniques for both timing and charge. Simulations were also performed based on projected radiogenic backgrounds and high-energy neutrino beam-line events which provide first estimates for the requirements of the digital back-end in both the quiescent and active states. Finally, based on these results from the simulations and prototypes presented here we discuss the nominal digital back-end readout constraints of a fully realized Q-Pix implementation for a DUNE-FD APA .

TABLE OF CONTENTS

LIST OF ILLUSTRATIONS

LIST OF TABLES

Chapter 1

INTRODUCTION

This chapter outlines and highlights useful background that will be explored in further detail in upcoming chapters as well as provides an outline for the thesis.

We begin with an overview of the standard model, and how both its success and short comings drive larger and more expensive detectors at the intensity frontier. To elucidate the issues at the forefront of the standard model we provide a brief history, with an emphasis on the detectors and experiments which helped lead to its formulation. Next, we become more specific and discuss DUNE which is an example of a new, large, and expensive detector which aims to push beyond the Standard Model. Finally, we finish this section on a discussion on the developments of new tracking detectors and highlight their relevance to the work presented here.

1.1 The State of Things: The Standard Model

What is the universe made of? What are the fundamental building blocks of matter? Since time immemorial thinkers have questioned the nature of the universe and wondered what the basic building blocks of nature are. The answer to these fundamental questions is the motivation for particle physics.

In the history of science, it is easily argued that the most successful of all models has been the Standard Model of physics. The Standard Model (SM) [1–3] was originally developed in mid to late 1970's, and is the model responsible for unifying the weak, strong, and electromagnetic forces together. It was gradually developed in the 1970's as a result of the boom of particle detectors in the middle and late 1960's. It has been made remarkable predictions about the existence of elusive neutrinos, quarks and vector bosons before their discovery, and more.

The comprehensive and extensive list of known particles as well as various cross-sections, lifetimes, and other known information can be found from the bi-annually published Particle Data Group (PDG) [4]. The SM has been experimentally tested to limits unlike any other theory.

In this section we briefly describe the SM and highlight some (certainly not all) key aspects of its formulation as understood today. The SM has stood the test of time, despite many known failures

and holes in its predictions. Therefore, we hope to elaborate a bit on its status involving predictions and unknwon parameters to help the reader better appreciate the significance of looking for physics beyond the SM.

The Basics of the Standard Model

The SM itself dictates what the fundamental constituents of matter and energy are. As any theory in science its purpose is to explain observed phenomena. In this case, the observed phenomena is (not) simply the origin of all observable particlesand their masses, and a desription for all observable interactions.

The interactions described by the standard model involve the fundamental particle interactions via three of the four known fundamental forces observed in nature: electromagnetic, weak, and strong forces. One of the current failings of the SM is its inability to incorporate a quantum description of gravity. The discussion of the re-normalization of quantum-gravity is beyond the scope of the work presented here, and so we only mention that it has to be achieved.

All currently known fundamental particles are represented in Fig. 1.1. These particles represent the today's best knowledge of the building blocks of all observed matter in the universe.

Quarks

The quarks represent particles in the top left of Figure 1.1.

Quarks are the fundamental particles which constitute the "normal" heavy particles, such as protons and neutrons. Quarks also have unique anti-particles partners of each other. As do all anti-particles, the anti-quark counter-parts have the same mass as the normal partners with all quantum numbers interchanged.

A unique feature of Quarks compared to the leptons is that no "free" Quark has ever been observed. Most commonly, the quarks combine in pairs or in triplets to make mesons or baryons, respectively. Even more complicated constituents can be made of additional quarks, such as tetra and penta quarks, so long as all of the quantum numbers are unique for each quark.

The mesons contain a quark and an anti-quark, whereas the baryons a contain three quarks. Collectively, all particles constituted by any combination of quarks are known as hadrons. In 1961 Murray Gell-Mann proposed his "eight-fold way" [6] which provided a method of grouping the hadrons.

2
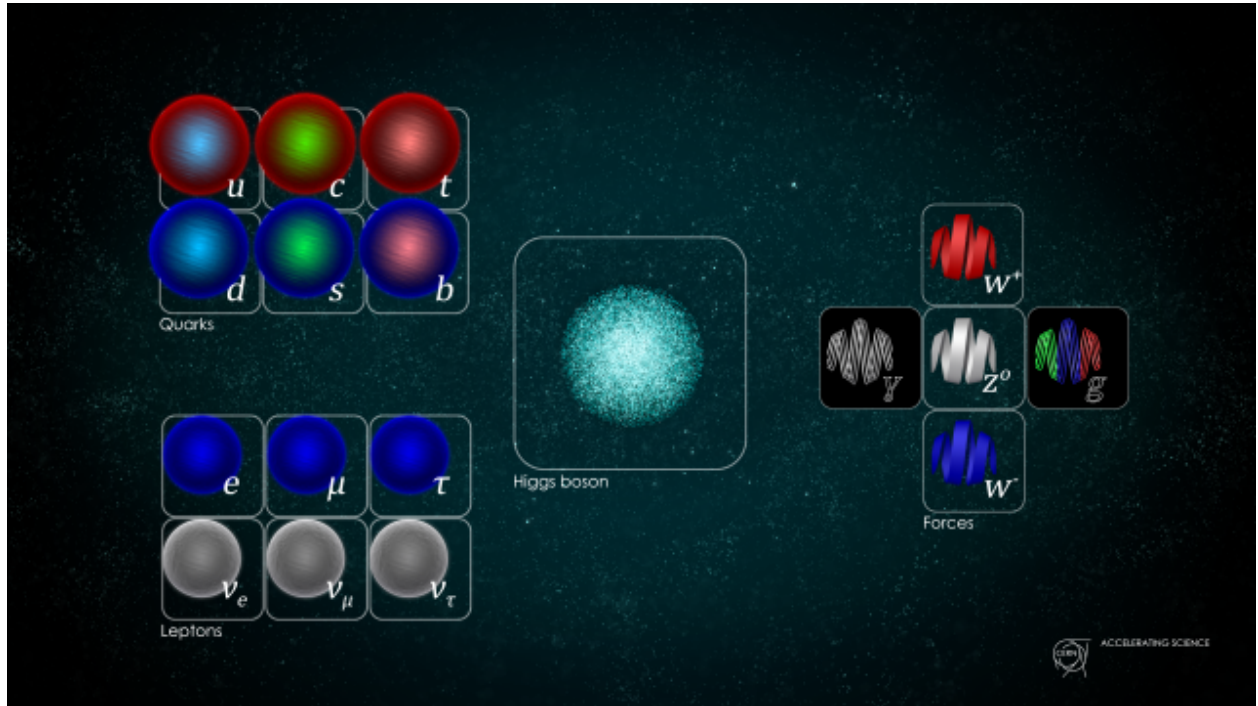
Figure 1.1: Image of Fundamental Particles in the Standard Model, taken from CERN website [5]. All known matter and particle interactions involves combinations of the particles listed here.

Since quarks are not freely observable a common place to infer their existence (and to create heavier hadrons) are in particle accelerators. The most well known particle accelerator is the Large Hadron Collider (LHC) in Geneva. These Particle accelerators generate extremely high energy ($\approx O(10TeV)$) protons which when collided can generate new composite hadrons of any mass so that the total energy is conserved.

Since quarks, due to their color, readily combine to create more easily observed composit particles. The Quark model was then propossed by Gell-Mann in 1964 [7]. This model is a group theory concept (known as SU(3) symmetry) and is the means for which the fundamental particles (quarks) combine into the composite particles (hadrons) which are more readily and easily measured today. Eventually experiments conducted at the Stanford Linear Accelerator (SLAC) between 1967-1973 verified the existence of these quarks and Gell-Mann won the Nobel Prize in 1969.

The rescue of the quark model came with the measurement of [8]. The J/psi particle indicated the existence of a fourth since then unmeasured quark, which we now know as the charm (c).

Quark	Charge	Mass (MeV)	Year Discovered	Ref.
up	$\frac{2}{3}$	2.16	1968	SLAC [9, 10]
down	$\frac{-1}{3}$	4.67	1968	SLAC [9, 10]
strange	$\frac{-1}{3}$	93.4	1968	SLAC [9, 10]
charm	$\frac{2}{3}$	1270	1974	SLAC [8]
bottom	$\frac{-1}{3}$	4180	1977	Fermilab [11]
top	$\frac{2}{3}$	173000	1995	Fermilab [12]

Table 1.1: Description of the discovery of quarks. Notice that as the mass increases for a particular quark the year of discovery also increases. This is a property of how we create and observe the quarks in our accelerators, and also the reason why physicists continue to want to build bigger ones. Interesting physics happens at higher and higher energies, which require larger and more expensive detectors to probe these energy scales. Note that the lighter quark masses are not well understood for other experimental reasons, and the presented data are rounded to three significant figures based on [4].

Leptons

The leptons represent particles in the bottom left of Figure 1.1.

The first lepton discovered, and the most easily recognized, is the electron which was discovered by J . Just like the quarks, the leptons come in three families (electron, μ, τ). Also like the quarks, the leptons have charge, mass, and flavour which means they can decay.

Unlike the quarks the leptonic particles do not have a color quantum number and therefore do not combine together to create composite particles. Additionally, free leptons are observed, e.g. the electron.

The most difficult to measure fundamental particles of within the SM are the neutrinos. This is because these leptons carry no net charge. However, since they carry flavour and can decay (or be absorbed) and they also carry their respective lepton number, the neutrinos in the family can be identified by measuring their partner.

For example, a common process to observe an anti-electron neutrino ($\hat{\nu}_e$) is through inverse beta-decay (IBD) following the reaction:

$$\hat{\nu}_e + p \rightarrow e^+ + n \tag{1.1}$$

This IBD reaction is a common measurement tool for identifying neutrinos because of the distinguisable detection signature of the produced particles. The position (e^+) annailates very quickly

Lepton	Charge	N_e	N_μ	N_τ
e^-	1	1	0	0
ν_e	0	1	0	0
μ	1	0	1	0
ν_μ	0	0	1	0
τ	1	0	0	1
ν_τ	0	0	0	1

Table 1.2: Description of the quantum numbers of the fundamental lepton families. There are three unique families within the leptons: electron, muon, and tau. The charge carrier as well as the neutrino each carry a value of one for this number. Their anti-particle counterparts carry -1 of this number.

$(\approx O(ns))$ and will produce back-to-back 511 keV photons. The produced neutron, on the other hand, wobbles around much longer ($O(us)$) before being captured, which produces scintillation light of energy proportional to the neutrons energy when captured.

The muon (μ) was discovered by Anderson and Neddermeyer in 1936 by observing cosmic ray showers [13].

The tau (τ) was discovered by SLAC in 1975 [14].

The first measurements of the neutrinos in each family were much harder than their charged partners. The electron neutrino (ν_e) and the muon neutrino (ν_μ) are observed in decay interactions.

The tau neutrino (ν_τ) was exceptionally difficult to measure. Like the previous neutrino partners, the ν_τ is discovered by looking for the creation of its partner (τ) during a CC interaction. As a comparison the τ has a lifetime of only 10^{-13} s whereas the muon life time $T_\mu \approx O(1\mu s)$ or seven orders of magnitude shorter!

The first successful experiment came in 2000 [15]. DONUT utilized a much more complicated emulsion detector to collect tracks from a 800 GeV proton beam offline. The exxperiment collected a total of 203 neutrino interactions, of which it found evidence for a total of only four interactions.

Forces - Vector Bosons

All forces within the standard model (electromagnetism, weak, and strong) are governed via a "carrier" particle. These carrier particles are represented on the center-right of 1.1.

Force	Scale	Theory	Carrier	Ref.
Strong	10	Chromodynamics	gluon	TASSO [16]
Electromagnetic	10^{-2}	Electrodynamics	photon	Planck?
Weak	10^{-13}	Flavourdynamics	$W^{\pm}$,Z	CERN [18],[19]
Gravity	10^{-42}	General Relativity	graviton	??

Table 1.3: Relative strength chart of the four fundamental fources of nature. Although gravity is not included within the SM it is included, as well as its theoretical force carrier the graviton.

The electromagnetic force is governed by particle exchanges of a photon. Other than perhaps gravity, which isn't explained by the SM, this is the most well known and described force. All particles which carry charge interact via this force. Therefore the neutrinos are the only particles within the quarks and leptons which do not interact at all with the electromagnetic force (this is why detecting them is so hard). The full theoretical description of this force is governed by Quantum-Electrodynamics (QED).

The weak-nuclear force is governed by particles exchanges of one of the three particles in the center: $W^{\pm}$ and Z. This force involves a change in flavor of a particle, and involves both quarks and leptons. It is also responsible for all decay processes. The theoretical description of these mechanics are called Quantum-Flavourdynamics (QFD).

The strong-nuclear force is governed by the exchange of the gluon (g). This force is responsible for color changes of matter and describes why nuclei are held together. Since this force only involves exchanges of a gluon, the leptons are therefore unaffected since these particles carry no color quantum number. The full theoretical description for the strong-nuclear force is Quantum-Chromodynamics (QCD).

The gluon was discovered in at the TASSO experiment 1979 [16, 17].

Measurements of the intermediate bosons were much harder. The $W^{\pm}$ boson were measured in 1983 [18]. Followed by the Z boson which was measured shortly afterwards in the same experiment [19].

Higgs - Scalar Boson

The last particle to be discovered in the SM was the Higgs particle. The Higgs particle was originally predicted in 1964 by Peter Higgs [20]. This particle is important to describe how mass is
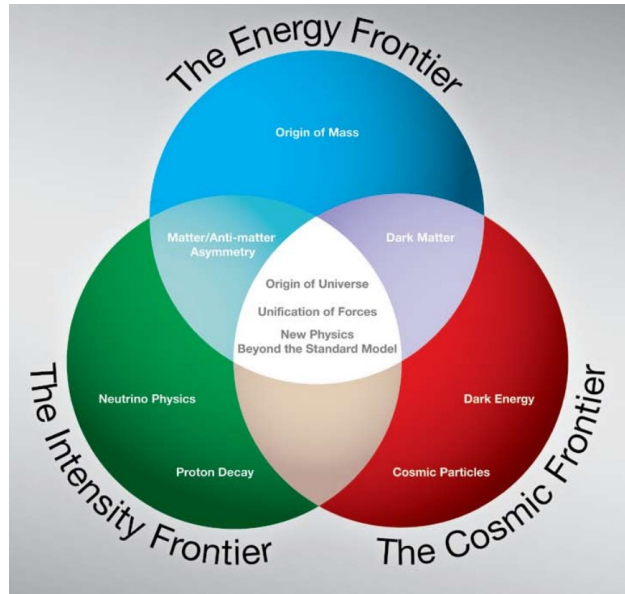
Figure 1.2: Image based on the 2008 P5 report [22]. The white text labeled within each frontier describes the search for some physics beyond the SM within that frontier.

given the the elementary particles described by the SM. Finally, in 2012 the Large Hadron Collider (LHC) was able to infer the massive Higgs particle [21].

1.2 The Problem: Moving Beyond the Standard Model

Despite its (SM) numerous achievements in predictive power and experimental verification we know today that it has crucial shortcomings. The Standard Model (SM) [1–3] has no ability to account for Dark Matter or Dark Energy in the universe, nor the distribution (or the hierarchy) of neutrino masses, nor is it able to relate how gravity interacts with the other fundamental forces of nature (Unification). It also doesn't account for some 'basic' properties it has, such as: why are there only three generations of leptonic particles (electron, muon, and tau)? These short-comings offer hints for where to search for physics. Physicists have known about these short comings from the conception of the Standard Model and have (to no avail) sought out what's next.

With a plethora of hints to search for New Physics (NP), it can be useful to organize the efforts of search. In 2008 the Particle Physics Project Prioritization Panel (P5) did just this and labeled the three frontiers of physics: the cosmological, energy, and intensity frontiers. Each of these frontiers offer different kinds of challenges and serve as guides to look for physics beyond the SM.

7

Searches at the Energy Frontier

The energy frontier is concerned with the origin of mass. The Large-Hadron Collider (LHC) [21] experiment is the archetypal experiment aimed at solving problems within this frontier. The LHC itself consists of other large-scale tracking and calioremtry experiments such as ATLAS [23] and CMS [24].

Large particle accelerators are used to generator source particles of ever increasing energy. Due to the conservation of mass, the higher the energy of the particle accelerated the higher the mass (energy) of the particles created after certain collisions can be.

There also exist lepton collidors [25] which offer unique areas of search along this frontier too. More detailed descriptions of such collider experiments are beyond the scope of the work presented here, and further reading may be pursued from the extremely detailed technical design reports cited here of Belle-II and the ATLAS experiments.

Searches at the Cosmological and Intensity Frontiers

The cosmological frontier aims to search for NP on extremely large time and distance scales by relying on observational techniques. Cosmological measurements have shown the that majority of the universe's matter is not visible to light, and so we call it dark matter. Additionally, the universe is expanding at an accelerated rate, which we can tell from the blueshift of distance galaxies. Likewise, cosmologists have also discovered that the universe is expanding due to some invisible energy in the universe, and so we call it dark energy.

The search for these dark causes of the universe lie within the realm of the cosmological frontier.

Dark energy currently resides as the explanation for the observed accelerated expansion of the universe. Dark matter is commonly used to explain the deviation of the rotational frequency of galaxy clusters.

The third (and final) frontier we'll discuss is the Intensity frontier. The Intensity Frontier of Physics ([22]) is one which today requires very large and very precise measurements to gain the statistics to declare an observation. In order to address the issues posed within this frontier the large scale detectors hunting for New Physics (NP) have continued to grow in size, energy sensitivity, and importantly cost: [26].

As compared to the energy frontier which normally relies on creating new particles from accelerators the Intensity Frontier often searches for rare events, like a proton decay.

Neutrino searches also lie within this frontier. Neutrinos are notoriously difficult to detect and measure since they can only be probed via the weak-nuclear force, and even then only indirectly since they carry no charge themselves.

How did we got here?

Many times since the early 20th century it was thought that the goal of physics was accomplished. However, during each of these moments of false triumph some new detector was built to take a new measurement; thus, the door to new understanding of nature is never closed. This section provides a brief and (necessarily) incomplete history of significant measurements and detector developments relevant to particle physics in the creation of the SM. In order to clear an obstacle, it is often helpful to remember the previous ones.

A Century of New Physics

At the turn of the 20th century particle physics was in its infancy. In 1900 Max Planck first introduces the concept of energy quanta for the first time concerning photons to eliminate the infamous ultra-violet catastrophe problem introduced by statistical mechanics. JJ Thomson used a single cathode-ray tube to discover the electron and the nucleus, and won for himself the Nobel Pize in 1906. Milikan's famous oil-drop experiment won him the Nobel Prize in 1923.

However, as each of these new discoveries solved problems only more questions were produced. Once the nucleus was discovered to contain only protons and neutrons, the natural question arose: what holds all of the positive charge together in the center. Thus, physicists cleverly named the new force which was stronger than the electromagnetic force: the Strong Force.

The bubble chamber was then invented in 1952 by Donald Glaser [27]. These detectors proved significant in the discover of the W and Z bosons and ultimately allowed the unification of the electromagnetic and weak forces to form the electroweak theory.

Next the spark chamber eventually lead to the gradual development of the wire-spark chamber. In 1968 Georges Charpak developed the Multi-Wire Proportional Chamber (MWPC) for which he (much later) won the Nobel Prize in 1992. From this key insight a new detector concept was made possible.

Finding Neutrinos

Hints at the existence of neutrinos began early last century. More than 100 years ago Chadwick was

able to show that the energy spectrum from a decaying electron was continuous [28]. This unknown cause of the spectrum even lead some physicists to belief that perhaps the conservation of energy was violated. Wolfgang Pauli instead predicted a particle which he originally called the neutron to also be a decay product, but not easily observable. This third particle in the decay would explain the energy spectrum of the electron. Quickly however the particle name neutron was taken by a different neutral particle in 1932 [29] The discovery of the neutron and the continuous spectrum of beta decay forced Pauli to come up with a new theory attempting to describe beta decay [30].

Originally physicists held little hope that such an elusive particle would ever be detected. However, the motivation to save this conservation law lead Wolfgang Pauli to the first prediction (1930) of the neutrino; the reason that the energy was a spectrum from the electron was that some of the energy was "taken up" by the neutrino. Finally, some 26 years later in 1956 was the first observation of the electron neutrino [31].

The discovery of the electron neutrino v_e was the first of the three families to be discovered. A few years later the first reactor neutrino (v_μ) was observed at Brookhaven National Laboratory (BNL) [32].

The first measurement of the τ neutrino (v_τ) happened much later in 2001 [15]. this detector used nuclear emulsions.

Daya Bay [33] has also established measurements of electron anti-neutrino ($\bar{v}_e$) disappearance.

After this first discovery is when the the answers, followed by more questions, came. Since then, many large-scale experiments have been dedicated to measuring the three generations of neutrinos. [33–40]

All reliable information we have about neutrinos come from these large scale detectors.

Originally the mass of the neutrino predicted by the SM was massless. That was until the Solar-neutrino anomaly measured significantly less neutrinos than predicted [41]. The solution for this was oscillation.

1.3 Modern Tracking Detectors

It is could said that any definition defining a "new" age of a types of detectors is subjective. Nevertheless, we proceed to define that modern particle detectors were the age that began to use modern electronics, or electronics after the development of the metal–oxide–semiconductor field-effect transistor (MOS-FET). If there was any invention which was able to drive the development of computers and measuring electronics, it was the transistor. Therefore, the beginning of the modern

particle detection age began with the transistor, and it saw to the end of the spark chamber and bubble chamber detectors.

Multi-Wire Proportional Chamber

The middle of the 20th century saw a dramatic increase in the ability and reduction of the cost of electronics. These (then) new electronics allowed for fast digitizing measurements of voltage or current. Thus, new propotional counter detectors were capable of using computers to do the measuring or counting of the events within the detector. The rate at particles could then be detected increased by orders of magnitude.

Using the fast digitizers and closely spaced wires Georges Charpak (1924-2010) created the first-Wire MWPC in 1968 [42]. This new detector was one which paved the way for modern detector development, for which Charpak won the 1992 Nobel Prize.

Time Projection Chambers

Time Projection Chambers (TPC) [43] have been shown to be extremely useful in high energy physics experiments due, in part, to their high resolution in both timing and spatial dimensions. This detector was originally used in the Position-Electron Project PEP-4 experiment which measured electron-positron collisions from the 29 GeV electron beam produced at the Stanford Linear Accelerator (SLAC). The first TPC design used high pressure gas and was able to measure 1000s of particle tracks per second (compared to 1-10) and provide full 3-D event reconstruction.

It did not take long for other experimentalists to generalize this concept to different elements or even to liquid.

Noble Gases and Time Projection Chambers

The technology of TPCs has greatly matured since their original inception. in many kinds of detectors across HEP. TPCs can also incorporate two phases of a substance (liquid and gas), called Dual Phase (DP) TPCs.

the Xenon-1T is a dark matter experiment which is a dual-phase TPC [44].

The LUX experiment is a single phase TPC also hunting for dark matter.

A specific kind of TCP is a Liquid Argon Time Projection Chamber (LArTPC) [46].

Recent work on LArTPCs ([47–49].)

Energy resolution of the LArTPCs within DUNE are still unknown to within a factor of 4 [50].
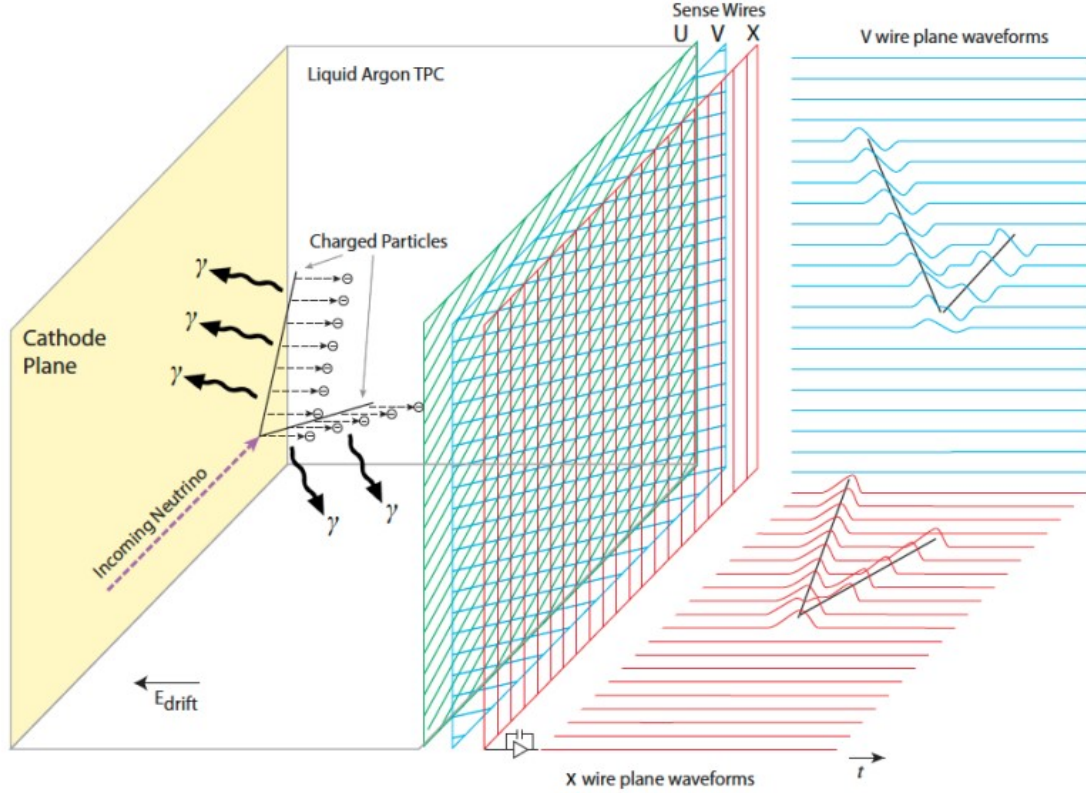
Figure 1.3: Image of a Time Projection Chamber (TPC). Charge is accumlated within the volume as ions are removed from the fidicial volume from another charged ion as it passes through the material. An uniform electric field drifts the free now electrons towards the anode plane. The collection and readout of charge on this anode plane is what is recorded within the detector. Image is taken from [45].

1.4 Ways Forward

Despite the passing of generations of detectors and developments in electronics the SM remains. For nearly 50 years now the SM is still our best model at describing nature as we know it, despite also knowing that there must be more. Here in this section we describe in some more detail current searches at the intensity frontier where physicists are looking to go beyond the SM.

We give special attention to neutrino oscillation at the end of this section since later chapters simulation studies will be based off results hoping to measure this effect.

Property	Symbol	Value	Unit
Density	ρ	1.3973	gcm^{-3}
Fano Factor	F	0.107	-
Dielectric Constant	ϵ	1.505	-
electron drift velocity	v_e	0.1601	cm/μs
Ionization Energy of single e^-	W_i	23.6	eV/e^-
Ionization Energy of single e^- from photon	W_{scint}	19.5	eV/γ
Minimum Specific energy loss	$(dE/dX)_{MIP}$	2.12	MeV/cm
Hadronic Interaction Length	λ_{int}	85.7	cm
Scintillation Emission Wavelength	λ_{scint}	128	nm
Longitudinal Diffusion Coeffecients	D_L	6.6270	cm^2/s
Transverse Diffusion Coeffecients	D_T	13.2327	cm^2/s

Table 1.4: Relevant Liquid Argon parameter information. Values are taken from [51], with temperature $T_s = 87K$ and electric field $E_f = 0.5kVcm^{-1}$.

Hadron Decay

Does a proton decay? This is the fundamental question for physicists looking at hadron decay. The SM predicts that the proton itself is stable, thus it should never decay. However, physicists know that the SM is itself not a complete theory since, among other reasons, it does not incporate gravity. Attempts to unify all of the fundamental forces of nature into one unified theory are considered Grand-Unified Theories (GUTs), and according to many GUTs the proton does, in fact, decay.

Current measurements on the proton lifetime indicate that its lifetime is on the order of magnitude (or above) 10^{34} years. Even at its most frequent, this is an exceedingly rare event considering that the lifetime of the universe is $\approx O(10^{10}yrs)$

Since these events are so rare, extremely large detectors with large numbers of protons inside of them are required to constantly observe many protons. An example of a second generation proton decay studies is the Imaging Cosmic and Rare Underground Signals(ICARUS) experiment [52].

There are at least two prominant decay chains that are expected to be dominant, depending on the Grand-Unification-Theory (GUT) that hopes to go beyond the SM. The first one is:

$$p^+ \rightarrow e^+ + \pi^0 + 2\gamma \tag{1.2}$$

This interaction is easily detectable in cherenkov based detectors due to the emission of both the gammas as well as the high energy of the emitted positron. In fact, the worlds best estimate for proton lifetime comes from this decay-chain [53].

Other Supersymmetric GUT models predict instead [54]:

$$p^+ \rightarrow K^+ + \nu \tag{1.3}$$

In this case the Kaon is generally moving too slow to be measurable by cherenkov detectors. However, a TPC style detectors are still sensitive to its signature charge deposition. This is an interesting reaction since the worlds best limits are currently provided by the Super-Kamiokande experiment, which is itself a cherenkov based detector in water.

These searches are interesting, if albeit difficult, both due to the rareness of such an event. If any detector was able to clearly measure even a single proton decay, that would provide direct evidence for physics beyond the SM. Future detectors that will continue to probe for nucleon decay are DUNE, Hyper-Kamiokande, and JUNO [26, 45, 55].

Supernova Studies

A supernova occurs when a massive star runs out of the necessary elemental fuel for fusion at its core. When this happens the inward pull of gravity due to the mass of the star overcomes the reduced outward pressure from the nuclear fusion.

It has been nearly 30 years since the last observed neutrinos from a galactic core collapse supernova, SN 1987A [56]. Sensitivity to supernova neutrinos is crucial for understanding the mechanisms that govern particles at these extreme densities and pressures. Interestingly, because neutrinos are so weakly interacting, it is possible to observe their signature and arrival before the photons arrival of a Type-II supernova.

The principal interaction chain observable in a TPC is:

$$\nu_e +^{40} Ar \rightarrow e^- +^{40} Kr^+ \tag{1.4}$$

A LArTPC is sensitive to ν_e by measuring the signture of both the e^- and $^{40}Kr^+$.

Neutrino Oscillation

Another possible route beyond the standard model are detailed studies of neutrinos.

Here we provide a very general description of a model to describing neutrino oscillation. We elucidate the measureable parameters which govern this oscillation and describe how these values are currently measured in experiments today.

Of all known particles the most elusive (hardest to detect and measure) is the neutrino. For this reason the least is known about the neutrino. What we do know about the neutrino is there are three flavors each associated with their leptonic partners: the electron, muon, and tau.

Tokai to Kamioka (T2k) [57] has well established neutrino oscillation measurements.

It came as a welcome shock that neutrino oscillation was first measured. This oscillation indicates that a neutrino as it moves through space can change its state; a electron neutrino can oscillate into a muon neutrino or even a tau neutrino. This happens because the mass eigenstate and flavor eigenstates which govern the neutrino are not equal.

The standard notation which relates the mass eigenstates (v_i) and flavor eigenstates (v_α) ,

$$v_i = U_{i\alpha} v_\alpha \tag{1.5}$$

$$\begin{pmatrix} v_e \\ v_\mu \\ v_\tau \end{pmatrix} = \begin{pmatrix} U_{e1}, U_{e2}, U_{e3} \\ U_{u1}, U_{u2}, U_{u3} \\ U_{\tau1}, U_{\tau2}, U_{\tau3} \end{pmatrix} \begin{pmatrix} v_1 \\ v_2 \\ v_3 \end{pmatrix} \tag{1.6}$$

The matrix elements within U_{li} represent the mixing coeffecients and are used to calculate the prability that a certain neutrino will oscillate from one family to another. We identify U_{ij} as the commonly known U_{PMNS} matrix, where PMNS stands for: Pontecorvo–Maki–Nakagawa–Sakata, or the four theorists who helped developed this convention. Luckily, there are not a total of nine free parameters within the SM that determine this. The U_{PMNS} matrix can be additionally rewritten following [58, 59] as:

$$U_{PMNS} = U_{sol} \times U_{rea} \times U_{atm} \times U_{maj} \tag{1.7}$$

After expanding the matrix representations, equation 1.4 becomes:

$$U_{PMNS} = \begin{pmatrix} 1 & 0 & 0 \\ 0 & C_{23} & S_{23} \\ 0 & -S_{23} & C_{23} \end{pmatrix} \times \begin{pmatrix} C_{13} & 0 & S_{13}e^{-1\delta_{cp}} \\ 0 & 1 & 0 \\ -S_{13}e^{-1\delta_{cp}} & 0 & C_{13} \end{pmatrix} \times \begin{pmatrix} C_{12} & S_{12} & 0 \\ -S_{12} & C_{12} & 0 \\ 0 & 0 & 1 \end{pmatrix} \times \begin{pmatrix} e^{i\alpha_1} & 0 & 0 \\ 0 & e^{i\alpha_2} & 0 \\ 0 & 0 & 1 \end{pmatrix}$$

(1.8)

We identify above the additional matrix components where historically these values are measured. Therefore, instead of nine unknown parameters for the SM, there are only six. The components C_{ij} and S_{ij} in the matrices are defined to be $\cos(\theta_{ij})$ and $\sin(\theta_{ij})$, respectively.

Then, the six parameters of the U_{PMNS} are identified as:

- θ_{13}, reactor measurements.

- θ_{12}, atmospheric measurements.

- θ_{23}, solar measurements.

- δ_{CP}, Charge-conjugation parity violation.

- α_1/α_2, The two Majorana Phase parameters.

The Majorana phases (α_i) are sensitive in experiments that can detect the Majorana nature of neutrions such as neutrinoless double beta decay. In neutrino oscillation measurements, these phases cancel out and not not measureable. Therefore, we ignore these two phases for the remainder of this work.

Next we demonstrate the calculation of the probability of oscillation from one mass eigenstate to another. Namely we calculate the probablity $P(\mu \rightarrow e)$ which is the probability of interest in a long beamline experiment. First we identify that equation 1.4 can be rewritten to isolate the flavor-eigenstate terms (v_α) by multiplying by the adjoint of the PMNS matrix (U^*_{PMNS}). Then the relationship between the mass and flavor eigenstates become:

$$v_\alpha = U^*_{PMNS}v_i \tag{1.9}$$

The value of interest is $P(\mu \rightarrow e)$. The probability to end up in state v_e beginning from v_μ is:

$$P(\mu \rightarrow e) = |\langle v_e | v_\mu \rangle|^2 \tag{1.10}$$

We then use equation 1.4 to represent the matrix elements of U_{PMNS} from v_e and v_μ to obtain:

$$P(\mu \rightarrow e) = |\sum_i U_{ei} U_{\mu i}^* e^{-iE_i t}|^2 = \sum_i |U_{ei} U_{\mu i}^*|^2 + 2\Re(\sum_{i>j} U_{ej}^* U_{\mu j} U_{ei} U_{\mu i}^* e^{-i\Delta_{ij} t}) \tag{1.11}$$

Where we identify that the cross terms introduce a phase difference shown as Δ_{ij} in the second term in equation 1.4. This represents the neutrino oscillation term and represents the difference in the mass states of the neutrinos:

$$\Delta_{ij} = (E_i - E_j) \tag{1.12}$$

The energy of the neutrino in each state can be approximated to first order following:

$$E_i = \sqrt{p^2 + m_i^2} \approx p + \frac{m_i^2}{2p} \tag{1.13}$$

The momentumum of all of the mass eigenstates is the constant. Then oscillation parameter becomes:

$$\Delta_{ij} \approx \frac{1}{2p}(m_i^2 - m_j^2) = \frac{\Delta m_{ij}^2}{2p} \tag{1.14}$$

Finally, the last two parameters which govern the neutrino oscillations are identified as the mass differences between the three mass states. Now, the frequency of the oscillation between neutrino states depends on the difference of the square their masses (Δm_{ij}^2), where three neutrino masses imply two independent differences. The mass differences provide two additional parameters are needed to fully describe neutrino mixing. The six values of interest and their current best known fits are shown in Table 1.4:

The the sign of m_{13} is unknown. This leads to two possible ordernigs of the masses, known as normal and inverted, NO and IO respectively. The normal ordering indicates that the masses of the
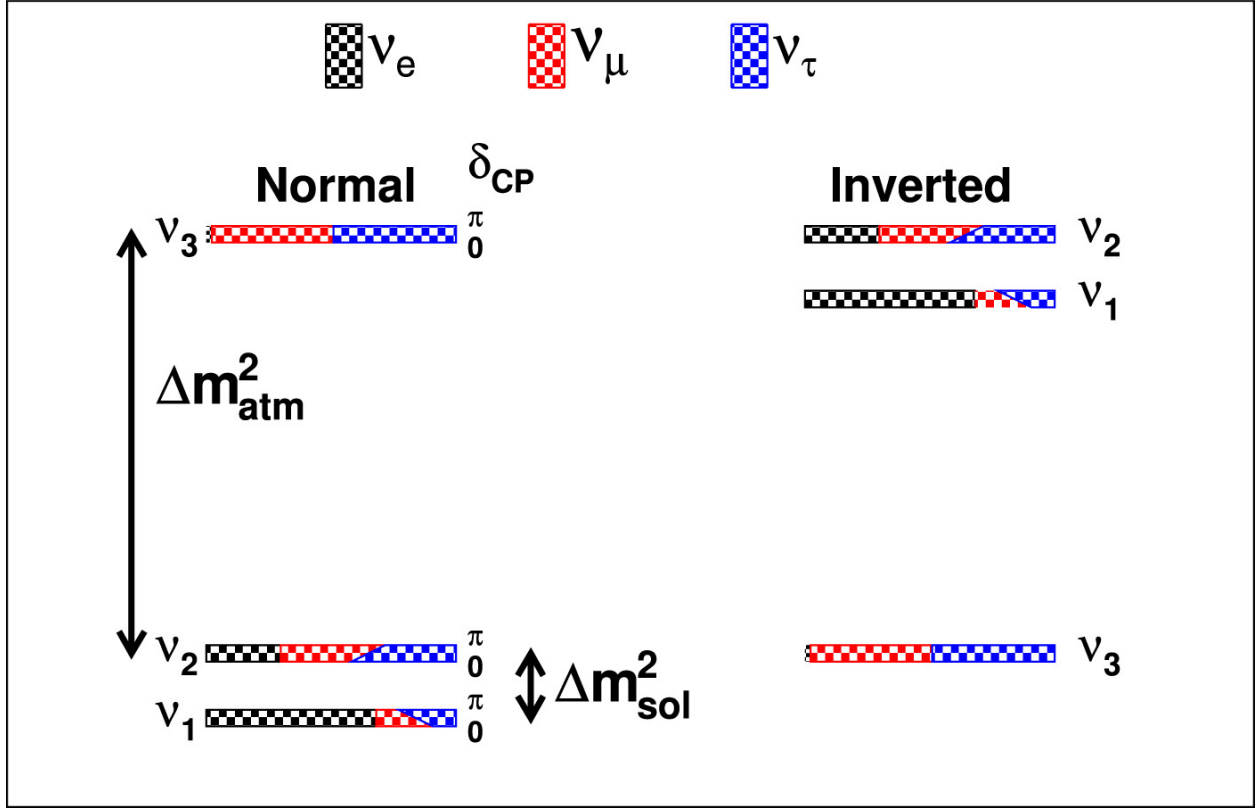
Figure 1.4: Representation of the mass hierarchy scales. This is a represntation of the two possible orderings of neutrino massses, due to the uncertain sign of m_{13}. It is also interesting to observe that the absolute mass scale is not measured since oscillation measurements only give difference mass squares. Image was taken from [60].

neutrinos follow the ordering of their charged partners. That is, NO implies a mass ordering of: $\nu_e < \nu_\mu < \nu_\tau$. Whereas, the IO has a mass ordering: $\nu_\tau < \nu_e < \nu_\mu$.

Neutrino oscillations in matter are slightly different than those in vacuum [61]. The Mikheyev-Smirnov-Wolfenstein (MSW) effect [62] also contributes to differening neutrino oscillations as they move through matter of varying density, which additionally complicated the calculation. The MSW effect also affects neutrinos differently than anti-neutrinos, which is useful for measuring δ_{cp}. This resonance affect for beam-line experiments affects ν_e in the case of normal mass ordering (NO), whereas in the case of inverted mass order (IO), the $\hat{\nu}_e$ experiences resonance and is thus more likely.

Paramater	Best Fit	Unit	Best Sorce
θ_{13}	$8.57^{+0.12}_{-0.12}$	na	Reactor
θ_{12}	$33.44^{+0.77}_{-0.74}$	Atmospheric	
θ_{23}	$49.2^{+0.9}_{-1.2}$	na	Solar
δ_{cp}	197^{+27}_{-24}	na	Atmospheric+Accelerator
Δm^2_{21}	$7.42^{0.21}_{-0.20}$	$10^{-5}eV^2$	Solar
Δm^2_{3l}	$2.517^{+0.026}_{-0.028}$	$10^{-3}eV^2$	Atmospheric

Table 1.5: Known Oscillation Parameters of Interest. Values are taken from the global fit [63]. The values shown assume normal mass ordering for neutrinos and include atmospheric Super-Kamikonde Data.

Paramater	Best Experiments	Type of Detector
θ_{13}		
θ_{12}		
θ_{23}		
δ_{cp}		
Δm^2_{21}		
Δm^2_{3l}		

Table 1.6: Comparison of which type of detectors are useful for measuring which values of neutrino oscillation.

1.5 Neutrino Tracking Detectors in the Current Century

Finally, in this last section we discuss the development of various upcoming detector technologies. There are many motivating pressures for new detectors to adopt pixelated designs. Below we discuss two contributing factors: the development of electronics and computing algorithms.

First, previously pixelated detectors have historically been more difficult because of the issues of cost and size regarding the number of readout channels. This is being addressed, in part, by the advent of newer, cheaper, and larger Field-Programmable-Gate Arrays (FPGAs). One method for reducing the electronic overhead required in pixelated detectors is to use digital multiplexing. Cheap, high channel FPGAs directly solve this problem. Other electronics development, such as the Silicon-Photomultiplier, offer much cheaper alternatives for large pixel counters compared to their historical counter-parts.

1.6 Future Detectors

[64] Another driving factor is the the development of Machine Learning (ML) algorithms, particularly Convectional Neural Network (CNN [65]). Recent industry has driven the need for CNNs to be able to correctly identify and label 2-D images of various kinds, and thus championed much of progress in this field and spawned many kinds of CNN algorithms. Recently, it has been shown how these kinds of algorithms extend into High Energy Physics (HEP) for particle identification. A major issue at the Intensity Frontier of physics is the sheer amount of data to store and process. These ML algorithms provied a developed tool to automate the analysis of huge amounts of data ($>> 1TB$) and have been shown to be quite accurate ($> 99\%$) at particle identification in LArTPCs.

Additional work has been performed in recent years which show that LArTPCs can also utilized a pixel-based readout [66], [67].

The end of the Standard Model era is inevitable. SM simply fails to account for physics with all major frontiers for physicists to accept its completeness; we know there is much and more to learn about nature.

The 20th century saw unprecedented progress in its sophistication of its detectors from ray tubes, to spark chambers, to proportional counters, and to huge (>20 km) particle accelerators. This century shows no signs holding any less promise than its predecessor. Continued development in electronics, computing, and analysis methods will lead to more and newer frontiers of physics.

The work presented in this introduction aims to not only encapsulate the massive progress particle physics has made since the electron's discovery, but also to server as a reminder of how extraordinarily surprising nature is. At every turn and at every point where physicists think they've arrived at the end (or at an impossible roadblock) there always remains more to discover. If we have learned anything, we have learned to knock and the door shall be opened.

The Deep Underground Neutrino Experiment

The Deep Underground Neutrino Experiment (DUNE) is a long-baseline neutrino beam experiment [45, 68–70]. DUNE is composed two detectors, a near detector (ND) and a far detector (FD) which are separated by a distance of 1300 km.

The ND is located at Fermilab and its purpose is to characterize the source neutrino beam created there. The ND serves many purposes. To name a few..TODO
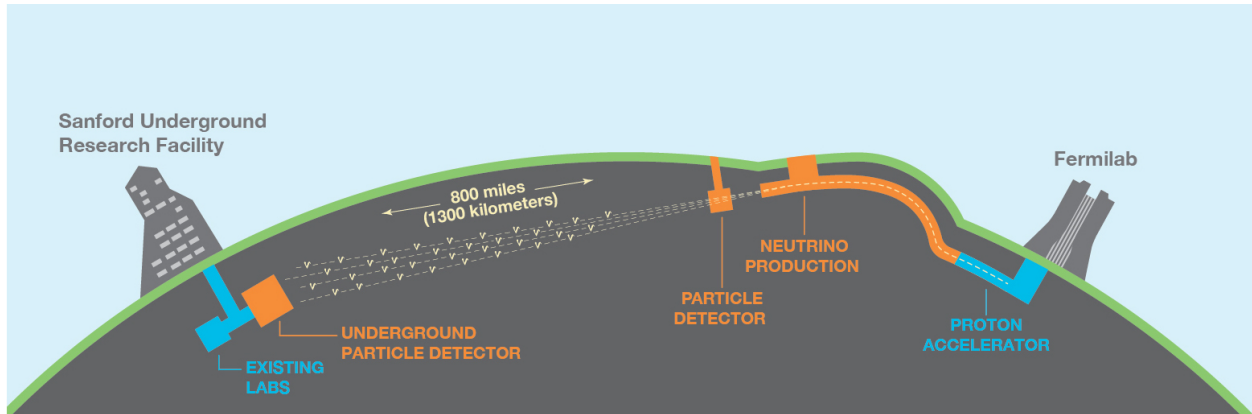
Figure 1.5: Representation of the Near and Far Detectors for the DUNE experiment. The Near Detector is located within the image labeled as the Particle Detector. One of the key purposes for the Near Detector is to tag outgoing particles from the proton beam. Image was taken from [71].

The FD will be placed underground at Sanford Underground Research Facility (SURF) and be approximately 1300 km away from the ND. This detector represents an enormous engineering challenge to place such large, cold, and complicated detector. The FD will be composed of up to four separate 10 kiloton modules.

DUNE plans to offer an incredibly rich searches across the sectors listed above 1.6. We briefly discuss the relevance of some the searches below, but more detailed reading can be pursued at [68].

Two of these four modules at least will use a known wire-based readout technology and a vertical drift-readout. The two remaining modules are considered modules of opportunity and their readout technology is yet unknown. A purpose of this dissertation is show the viability of a novel readout technology.

DUNE has three main science goals, all of which are geared towards pushing beyond the standard model:

- Hadron Decay 1.4

- Core-collapse Supernovae 1.4

- Neutrino Oscillation 1.4

We will discuss the relevance of each of these items, and in chapter 2 where we will further discuss how the work presented here relates to each of these topics.

Conventional horizontal drift detection for foreseeable DUNE modules are already considered possible for lengths up to 6.5m [72].

Chapter 2

A NOVEL READOUT TECHNIQUE FOR TPCS: Q-PIX

In this chapter we introduce a novel pixel-based readout concept for TPCs. Pixel based readouts offer several advantages over the traditional wire readout [73]. A key improvement offered from pixelization is true 3-D image reconstruction. This allows for sharper vertex reconstruction, thereby improving the overall resolution of DUNE and decreasing the required time for a NP measurement.

Other advantages are ease of data analysis and a reduction in total data storage. A pixel based readout automatically records two of the three spatial dimensions, and thereby provides for simpler analysis. Additionally, the pixelated readout method presented here cuts the total required data storage and data acquisition rate (without loss to precision) by several orders of magnitude.

However, the advantages also come with the cost of increased design complexity as the number of readout channels increases by more than three orders of magnitude. The traditional wire based readout within a DUNE module will include hundreds to thousands of channels, whereas a full DUNE module with a pixel-based readout will have 10's of millions of channels. This number of required channels to be stably readout during DUNE's expected lifetime ($\approx$ 20 years), where the electronics continually operate at liquid argon temperatures is likely the largest hurtle for a pixel-based design. The aim of this dissertation is to address the channel-size problem.

2.1   Q-Pix: The Circuit Level Design

The fundamental readout circuit (2.1) was first introduced by Nygren and Mei [74]. The principle of the front-end circuit operates on measuring the the time of the output of a trigger which is connected to an integrating capacitor circuit. The key difference of this readout circuit is that the measured value is time, not voltage or charge. Such a design choice then allows this readout to only provided data when there is charge.

The circuit input is connected to the anode of a TPC where drifted electron charge accumulates. Voltage is then built up from the charge stored on the pixel based on the capacitance according to the equation:

$$Q_i = C_i V_i \tag{2.1}$$
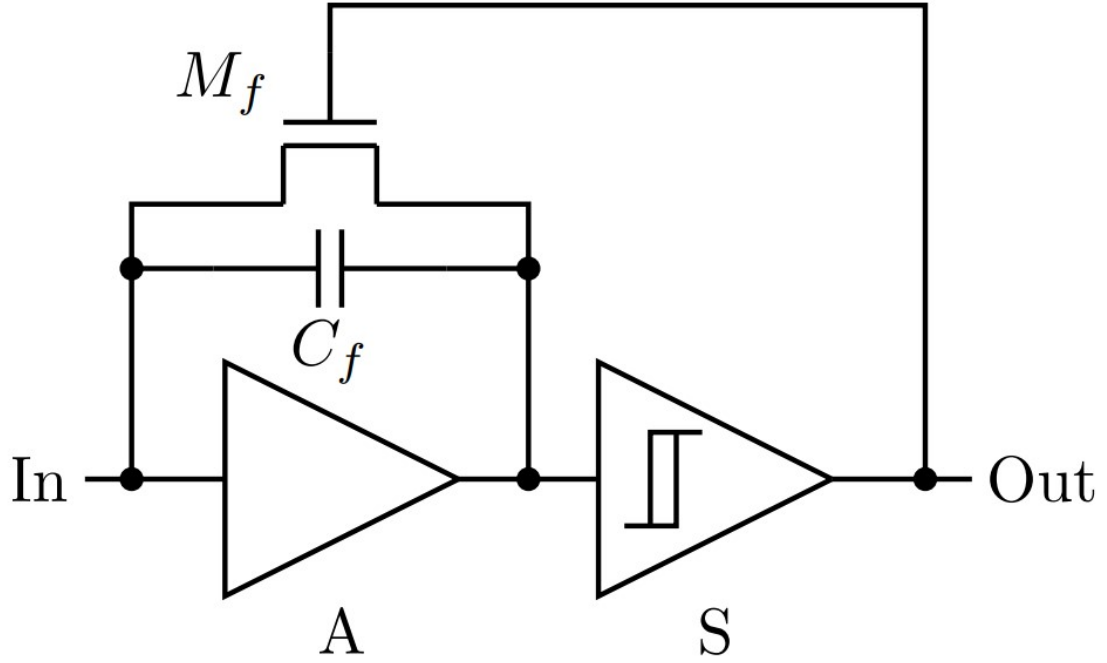
Figure 2.1: Image of Basic Q-Pix Readout circuit. Currently this front-end circuit is being designed as custom analog ASIC which has 16 channels. Image is taken from [74].

After the capacitor voltage (V_i) exceeds a set threshold value the schmitt trigger activates. The time of the trigger output is recorded by a digital logic which encodes this data as a 32 bit value. Since the capacitor reset happens at the same time as the issued trigger the digitally-recorded value is the reset time.

This timestamp value is recorded against a free running local oscillator (f_o = 30MHz). The number of free running clocks in the entire system is expected to be the number of channels (N_c) divided by the number of digitally multiplexed channels (N_d), which are taken to be 16.

Waveforms from Time Resets

Here we describe the basic principle of reconstructing the input current from a collection of reset measurements. The key insight for this readout technology is that time (instead of voltage as in a MWPC) is recorded. Therefore, measurements only taken place when there is enough charge to cause a reset which prevents continuous measurements during periods of long dead time. This

concept follows the detector concept of least action in that all measurements are detector responses.

A measurement of a reset indicates that a certain amount of charge was discharged from the integrating capacitor. Since total charge is conserved (and assume drift current around the integrator is small compared to backgrounds), we can say that the total amount of charge that accumulates onto the pixel is equal to total amount of charge discharged from each reset, plus any residual charge still on the pixel. Therefore, we can relate the total accumulated charge to the total charge discharged with the following equation:

$$Q_{in}(t) = Q_{out}(t) + Q_c(t) \tag{2.2}$$

eq:qin)

If we assume that each reset removes the same amount of charge during each reset then we can rewrite the total charge out (Q_{out}) in terms of the integer number of resets at time t ($N(t)$):

$$Q_{out}(t) = Q_o N(t) \tag{2.3}$$

eq:qout)

Where Q_o is the fixed amount of charge discharged during each reset. Equation **??** then can give us the measured current by definition ($I = \frac{dQ}{dt}$):

$$I_o = \frac{d}{dt}(Q_o \times N(t)) = Q_o \frac{dN}{dt} = \frac{Q_o f_o}{N_{clk}} \tag{2.4}$$

eq:irecon)

Where we identify $\frac{dN}{dt} = \frac{f_o}{N_{clk}}$ as the as the clock frequency (f_o) of the local clock and the difference between the two resets. Equation **??** can be used to determine the maximum current with the digital clock frequency by noting that the minimal value of N_{clk} is one. We take as the nominal expected frequency (30 MHz), capacitance (1 fF), and voltage (1 V) values to calculate an approximate max current, I_{max}:

$$I_{max} \approx 1\ fF * 1\ V * 30 * 10^6 MHz \approx 30\ nA \tag{2.5}$$

We note that 30 nA is much greater than the expected background current from Ar^{39} ($O(10^{-18})A$). However, more interesting events deposit more more charge. We can use the average drift speed of

25

electrons in a LArTPC to estimate the maximum charge density such a configuration is sensitive to:

$$\lambda_{max} = \frac{dQ}{dL} = \frac{dQ}{dt} / \frac{dx}{dt} = \frac{I_{max}}{v_{drift}} \tag{2.6}$$

We use a nominal v_{drift} speed of 1.6 mm / μs, and convert to SI units to obtain λ_{max} in equation 2.1:

$$\lambda_{max} = \frac{3 * 10^{-8} A}{1600 \frac{m}{s}} = 1.875 * 10^{-11} \frac{C}{m} \approx 19 \frac{nC}{mm} \tag{2.7}$$

We can now use this result to calculate a maximum $\frac{dE}{dx}$ measurement:

$$\frac{dE}{dx}_{max} = \frac{dQ}{dx}_{max} \frac{dE}{dQ} = \lambda_{max} \frac{dE}{dQ} \tag{2.8}$$

We can take the ionization energy of Ar^{39} to be $W_{ion} \approx 23.6eV$, then:

$$W_{ion} = \frac{23.6eV}{e^-}$$

and

$$Q = 1.602 * 10^{-19} C$$

Then $\frac{dE}{dQ}$ becomes:

$$\frac{dE}{dQ} = \frac{23.6eV}{1.602 \times 10^{-19} C} \tag{2.9}$$

Finally, we calculate the result of equation **??** and convert to units of $\frac{GeV}{mm}$.

$$\frac{dE}{dx}_{max} = 1.875 \times 10^{-11} \frac{C}{m} \times \frac{23.6eV}{1.602 \times 10^{-19} C} \approx 2.76 \frac{MeV}{mm} \tag{2.10}$$

Next we aim to provide an estimate on the lower limit of detection for an event. What follows provides a rough estimate for a potential lower bound on signal identification in the analysis, and note that a more thorough investigation of a true lower limit would require more work and beyond the scope of the work presented here.

First, we take as a lower bound estimate that any signal detection for an event purely based on charge reconstruction must provide more resets than background due to Ar^{39} beta-decay. Since the background rate from the dominate source is expected to provide resets of frequency $\approx$ 1Hz, an order of magnitude estimate for the minimal detectable current can be measured if we assume a signal-to-noise ratio (S/N) of 10. Then, a detectable signal rate should deposit enough charge to trigger a reset within a time window of $\approx$ 0.1s.

Following equation **??**;

$$I_{min} \approx \frac{1\ fF \times 1\ V}{0.1s} \approx 10\ \text{fA} \tag{2.11}$$

We use I_{min} to calculate an average charge line-density above the pixel, and again assume a constant drift speed, $v_e \approx 0.1601\text{cm}/\mu\text{s}$, from table 1.3.

$$\lambda_{min} = \frac{10^{-14}A}{1600\frac{m}{s}} = 6.25 \times 10^{-18}\frac{C}{m} \approx 6.25\frac{aC}{m} \tag{2.12}$$

Finally, we calculate the minimum $\frac{dE}{dX}$ following 2.1:

$$\frac{dE}{dx}_{min} = 6.25 \times 10^{-18}\frac{C}{m} \times \frac{23.6eV}{1.602 \times 10^{-19}C} \approx 0.921\frac{eV}{mm} \tag{2.13}$$

Pixel Calibration

Calibration measurements are essential for any detector, as they provide a means to differentiate signal from noise. Here we briefly describe an automatic use of existing Ar^{39} decays as a source of calibration at the pixel level. A full discussion of simulations using backgrounds is found in 3.

The target volume (LAr) is stable nobel but still provides a quiescent background from the charge deposited β decay ($\approx$ 6MeV). The total volume continually observed by any pixel a drift distance $\approx$ 3.5m yields an average reset on the order of 10s of seconds $O(10^1)$. This value is much lower
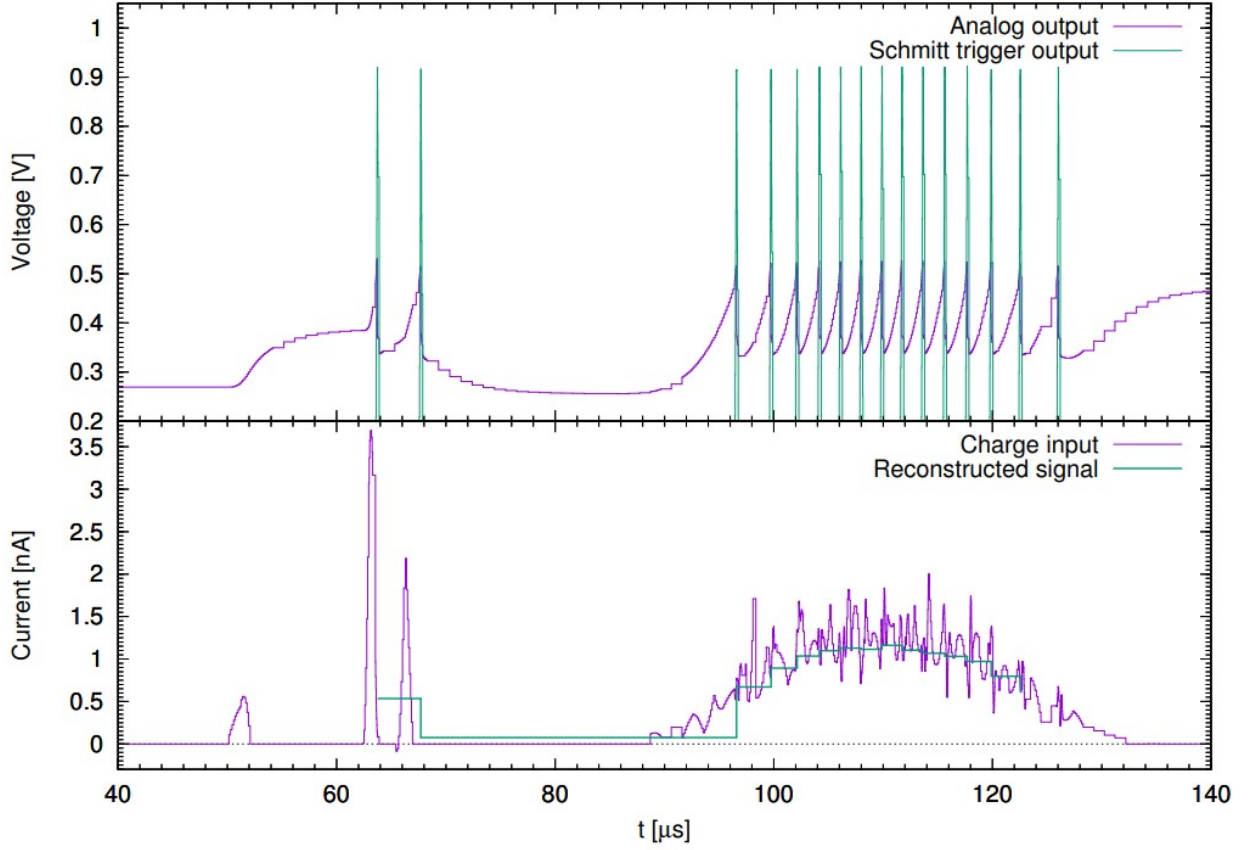
Figure 2.2: Example reconstruction of the reset time difference (RTD) based on the Q-Pix readout design. Image is taken from [74].

than the wrap-around rate of the 32-bit sample clock, which in practice will provide continually increasing reset values and prevent errors in identifying the correct reset time.

The pixel leevl value which needs to be calibrated is the pixel's response to an input charge Q_{in} in equation 2.1. The capacitance (C_i) for each pixel is a systematic which can be calibrated periodically using the background current from Ar^{39} decay. Given some stable input charge, there is a known number of reset measurements to calibrate against.

LAr purity over the detector volume is essential for background calibration. Differents in purity, electric, and maagnetic fields affect the major contributions to charge loss in the LAr: recombination, lifetime, and diffusion.
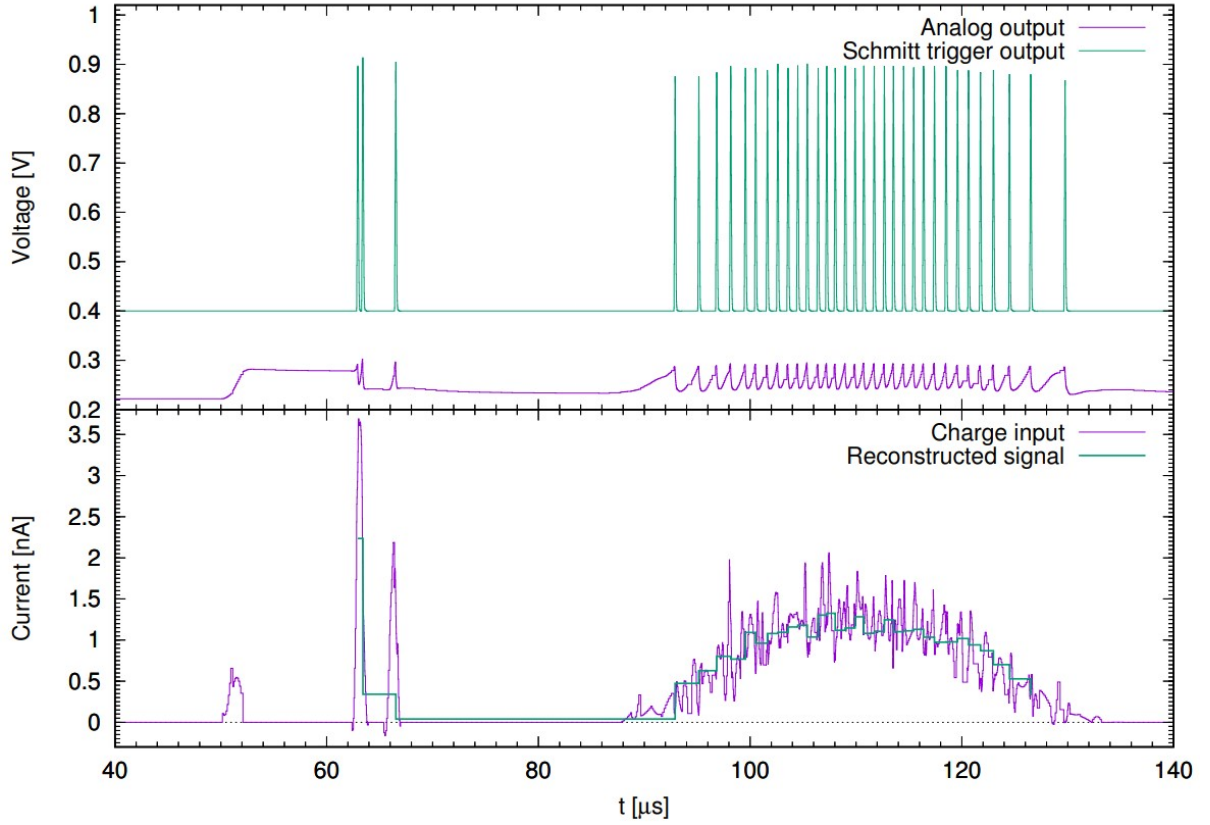
Figure 2.3: Example reconstruction of the reset time difference (RTD) based on the Q-Pix readout design. delta-Q was chosen to be $0.3 fC$. Image is taken from [74].

Making a 3-D Image

One of the important features of a TPC is the ability to reconstruct full 3-D images. The intended benefit of a pixelated readout on any TPC is to show that there are improvements to reconstruction of these 3-D images.

In order to reconstruct the image of the interaction from a set of data above the pixel the required data are the reset time at a pixel i (T_{ri}), event time (T_e), and the pixel ID. We assume that T_e (as is normally used to tag events in TPCs) uses a trigger time from a secondary PMT system from the scintillation light produced by the interaction to tag an event of interest. Since the scintillation photons travel much faster than the drift electrons, we can use the T_e as the starting time.

The pixel ID of each reset gives two of the three remaining coordinates ($\hat{x}$ and $\hat{y}$). The last coordinate ($\hat{z}$) is reconstructed using T_{ri}.

Since the drift velocity of the electrons (v_e) is constant in a TPC the distance that the electrons

traveled to reach the anode plane ($\hat{z}$) is determined based on only the drift time:

$$z = v_e * T_{drift} \tag{2.14}$$

However, this drift time is measured directly from the difference between the event time (T_e) and the reset time for this pixel (T_{ri}).

$$T_{drift} = T_{ri} - T_e \tag{2.15}$$

The drift distance in equation (2.1) becomes:

$$z = v_e * (T_{ri} - T_e) \tag{2.16}$$

Bad Scenarios

Here we briefly describe potential issues of the readout circuit presented here.

Near Maximum Reset Rate

Equation 2.1 relates the maximum measurable current (I_{max}) in a QPix system to the frequency of a digital clock.

The general relationship for the curret is given in equation 2.1. This can be rewritten explicitly in terms of the number of measured clock counts at the remote ASIC:

$$I_r(N_{clk}) = \frac{Q_o f_o}{N_{clk}} \tag{2.17}$$

Where f_o is the nominal frequency of the free running remote clock, and N_{clk} is the 32-bit encoded timestamp.

We note here that because N_{clk} can only take positive integer values that there can be large uncertainty in the measured currents between the maximum and half of the maximum. That is since $I(t) \simeq 1/N_{clk}$, explicitly measured currents can only be discrete and have large variance for small N_{clk}.

However, these discrete uncertainties can be accounted for after digital processing. An example of a periodic artificial input current of with $I \approx I_{max}/10$ is shown below in Figure 2.1. The reconstructed charge over time is shown in Figure 2.5.
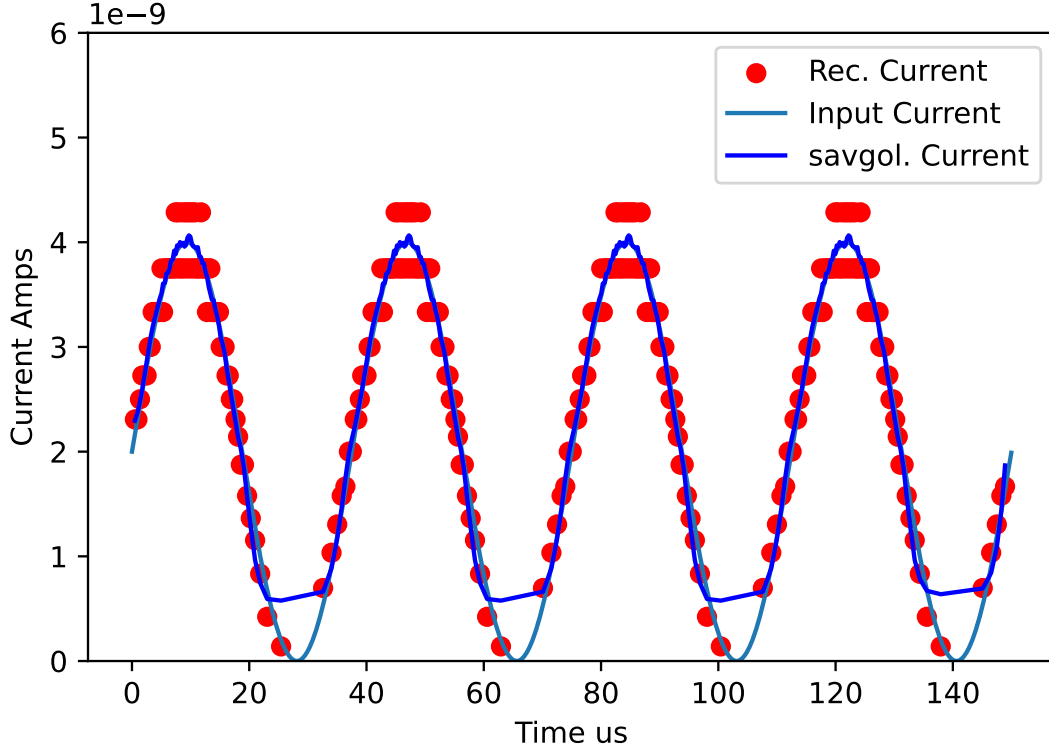
Figure 2.4: Arbitrary sin-wave based current input. Maximum amplitude is chosen to be close to I_{max}. Reset Charge is chosen to be 1 fC and digital clock frequency of 30 MHz. Since the amplitude is close to the maximum, and the clock measuremets are necessarily discrete, the exact current can not be measured from reset-to-reset. However, an example of a savgol filter is performed on the resets after the fact, shown in blue, with near agreement of the large input. An use-case of this kind of digital filtering would be applied to large current values only, and not for low current inputs, where the pure timestamp difference provides better results.

Discussion of Uncertainties

The uncertainty for the two transverse coordinates ($\hat{x}$ and $\hat{y}$) come from the pixel size. If we assume the electric field to be uniform, on average, across all $O(10^7)$ pixels in an APA, then the charge drift will be uniformly distributed over the pixel size. Then, the pixel dimensions determine the resolution: $\frac{3mm}{\sqrt{12}} \approx 0.87mm$.

The two remaining coordinates to reconstruct tracking are drift distance, $\hat{z}$, and then time the charge was deposited, T_{ei}. The measurement of $\hat{z}$ is based on equation 2.1. Expanding the uncertainties

((a)) CDF   ((b)) Difference
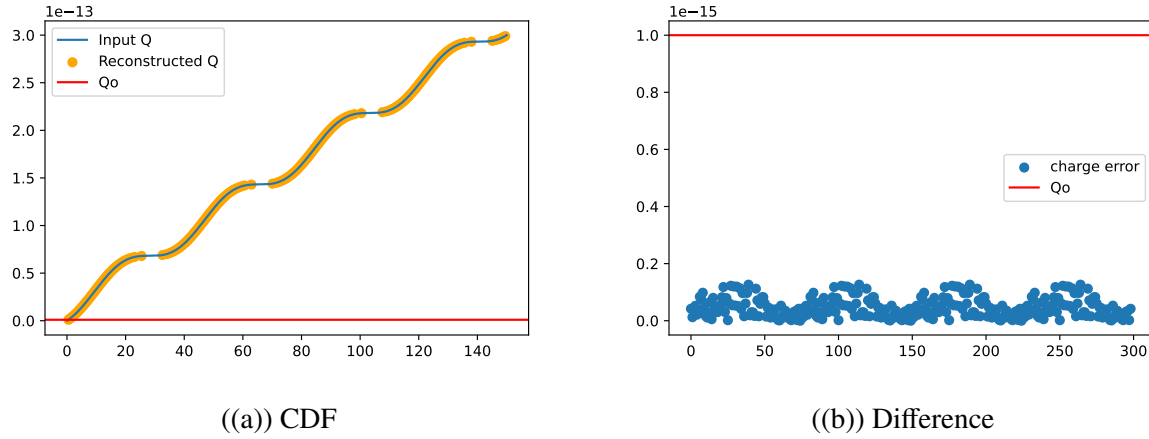
Figure 2.5: Reconstruction of Sub figures CDF of charge as a function of time (a) and difference (b).

based on this equation, and assuming v_e to be a constant, gives us a relation for $\sigma_{\hat{z}}$ to be:

$$\sigma_{\hat{z}} = v_e(\sigma_{T_{ei}} + \sigma_{T_e}) \tag{2.18}$$

Where $\sigma_{T_{ei}}$ and σ_{T_e} are the uncertainties for the reconstructed charge arrival time and the event time, respectively. Of these two, only $\sigma_{T_{ei}}$ depends on the reconstructed charge value; T_e can be provided as an external trigger, such as a photonics system which uses scintillation photons. Such a system can reasonably expected to have a much smaller uncertainty than $\sigma_{T_{ei}}$ since its timescale (ns) is three orders of magnitude smaller.

Therefore, to reasonable approximation $\sigma_{\hat{z}}$ is:

$$\sigma_{\hat{z}} \approx v_e\sigma_{T_{ei}} \tag{2.19}$$

Equation 2.1 relates the uncertainties of the last two coordinates which define a total event reconstruction. A full treatment of the uncertainty in time ($\sigma_{T_{ei}}$) depends on the uncertainty of the measurement of the timestamps for each remote ASIC in a tile, as well as the charge per reset (Q_o) and nominal frequency of the ASIC (f_o). The full treatment to analyze the uncertainty of f_o is the goal of this work and the details are provided in Chapter 4. The measurement of the uncertainty provided by the charge (Q_o) depends strictly on the analog front-end, which is beyond the scope of the work presented here.

We can provide here, however, an order of magnitude estimation based on equation **??**, if we consider only the contribution of the uncertainty due to the measurement of time which depends on the number of clocks recorded since the last reset (N_{clk}). Since the measurement of the input current is inversely proportional to N_{clk}, the percent uncertainty of the current measurement is proportional to the percent uncertainty in the timestamp measurement.

A 1% measurement of error can be calculated using a standard percent error definition, and by noting that the maximmal error happens when a true current should record a value between $N_{clk} + 1$ and N_{clk} counts. A maximal error of a measured current would happen if the current provides just shy the amount of charge to trigger a reset in N_{clk} cycles and instead the recorded reset occurs on the next clock, $N_{clk} + 1$. The worst case true measurement should be:

$$N_{true} = \frac{1}{N_{clk}} \tag{2.20}$$

We can then directly apply percent error:

$$error = \frac{\frac{1}{N_{true}} - \frac{1}{N_{clk}+1}}{N_{true}} \tag{2.21}$$

Plugging in the value N_{true} from equation 2.1 and simplifying gives:

$$error = \frac{1}{N_{clk} + 1} \tag{2.22}$$

Equation 2.1 provides a general formula for calculating the maximal error due to the discretization of the timestamp measurement. Then, we can solve for N_{clk} to determine how many clock cycles must occur between two resets for a 1% error (error $= \frac{1}{100}$):

$$N_{clk} \approx 100 \tag{2.23}$$

Then after 100 clock cycles, the worst possible measurement of the current is still within 1%. 100 clocks cycles for a 30 MHz clock yields measured drift time $t_{drift} \approx 3.33~\mu s$. The drift, v_{e^-} is $\approx$ 1.6 $\frac{mm}{\mu s}$, multiplied by the time gives the drift distance, known to within 1%:

$$\hat{z} = v_{e^-} t_{drift} \approx 3.33 \cdot 1.6 = 5.33 \text{mm} \pm 0.05 \text{mm} \tag{2.24}$$

We can rewrite equation 2.1 explicitly in terms of N_{clk} to get a worst case:

$$\hat{z} = v_{e^-} \frac{N_{clk}}{f_o} \qquad (2.25)$$

The maximal percent error in the drift distance due to timing increases as N_{clk} decreases, however because the drift distance is also calcuated using.

2.2 How Q-Pix fits into a DUNE APA

Here we briefly describe QPix system requirements at DUNE module size (10 kt). A full technical design report for a kt module implementing QPix is clearly beyond the scope of the work presented here, yet we still offer comments on the requirements, particularly on the digital back-end related to a DUNE APA.

DUNE's Anode Plane Assemblies (APA) full description can be found at [70]. Expected noise level of 1000 e^-. Sampling frequency of 12 bit ADCs is 12 MHz. Expect to collect 20-30 ke^- per channel for a minimum ionizing particle. Large signals require a linear reponse of 500 ke^-, and ensures that fewer than 10% of beam events experience saturation.

Dune APA takes 20 Front-End-Motherboards (FEMBs), to digitize a total of 128 wires. 40 wires are taken from the U and V (induction) layers, and 48 wires are taken from the X (conduction) layer. The reason for this distribution is simply that that the X layer has a total of 980 wires per APA, where the U/V layers have 800 wires.

Three ASICs are responsible for collecting the charge as it passes between the wires and sending it out of the cryostat. The first ASIC is a waveform-shaping and amplification ASIC. The second ASIC is the ADC ASIC and is reponsible for converting the analoge signal to digital. The final ASIC, called the COLDATA ASIC, merges the data streams from the previous ASICs and is responsible for communication between the motherboard and the outside world. Maximum expected data collection is to exceed no more than 30 PB/year, which corresponds roughly to $\approx 1 Gb/s$ of continuous collection.

Each 10 kT module consists of 150 APAs. Dune expects to draw less than 50 mW per channel, and less than 1% dead channels.

Each APA is 6.324 m × 2.316 m, for a total area of 14.646 m^2. Therefore, the expected channel count of a QPix APA is

$$N_{pix} = 14.646m^2 * \frac{1\,pixel}{4mm^2} * \frac{1000^2 mm^2}{m^2} = 915399 \tag{2.26}$$

To have a comparable power draw compared to DUNE, which has 2560 channels, then QPix would need less than $\approx 140\mu W$ of power draw per channel. Too much energy disappated in the LAr creates bubbles which is a high voltage (HV) discharge risk. The total channel count for a 10 kT module is based on 150 DUNE-APAs or $2560 \times 150 = 384000$.

Thus, the number of extra analog channels that QPix is required to measure, compared to the typical wire readout, increases by a factor of $915399/2560 \approx 357$. This is an increase of $O(10^3)A$ orders of magnitude.

QPix instead offes conversion from analog (charge) to digital (32 bit time) signals on the front-end ASIC. These front-end ASICs would be arrayed in tiles, and the tiles themselves would spread out to cover the entire area of an APA. Each tile would interface with a single FPGA chip would would concentrate the digital data for each tile; we refer to this FPGA as the DAQ-Node (DN). Then, each DAQ-Node interfaces with at least a single concentrator FPGA that sends the digital data to the Warm-Interface-Cards (WIC) out of the cold electronics (CE). The final concentrator FPGA we refer to as the Super-DAQ-node (SDN).

The exact description and characteriziation of the WIC for a QPix depends on the final implementation of the SDN and is thus beyond the scope of the presented here.

2.3   Digital-Backend Requirements

We consider that the digital blocks responsible for digitizing the reset to have a nominal frequency of $\approx 30MHz$. Therefore, the minimum time before the recorded timestamp value resets is calculated by:

$$T_{loop} = \frac{2^{32}}{30 \times 10^6} \approx 143\,seconds \tag{2.27}$$

This time (T_{loop}) indicates the minimum reset time to occur within each responsible digital block. Since this time is much greater than the antipcated reset rates to be produced from backgrounds,
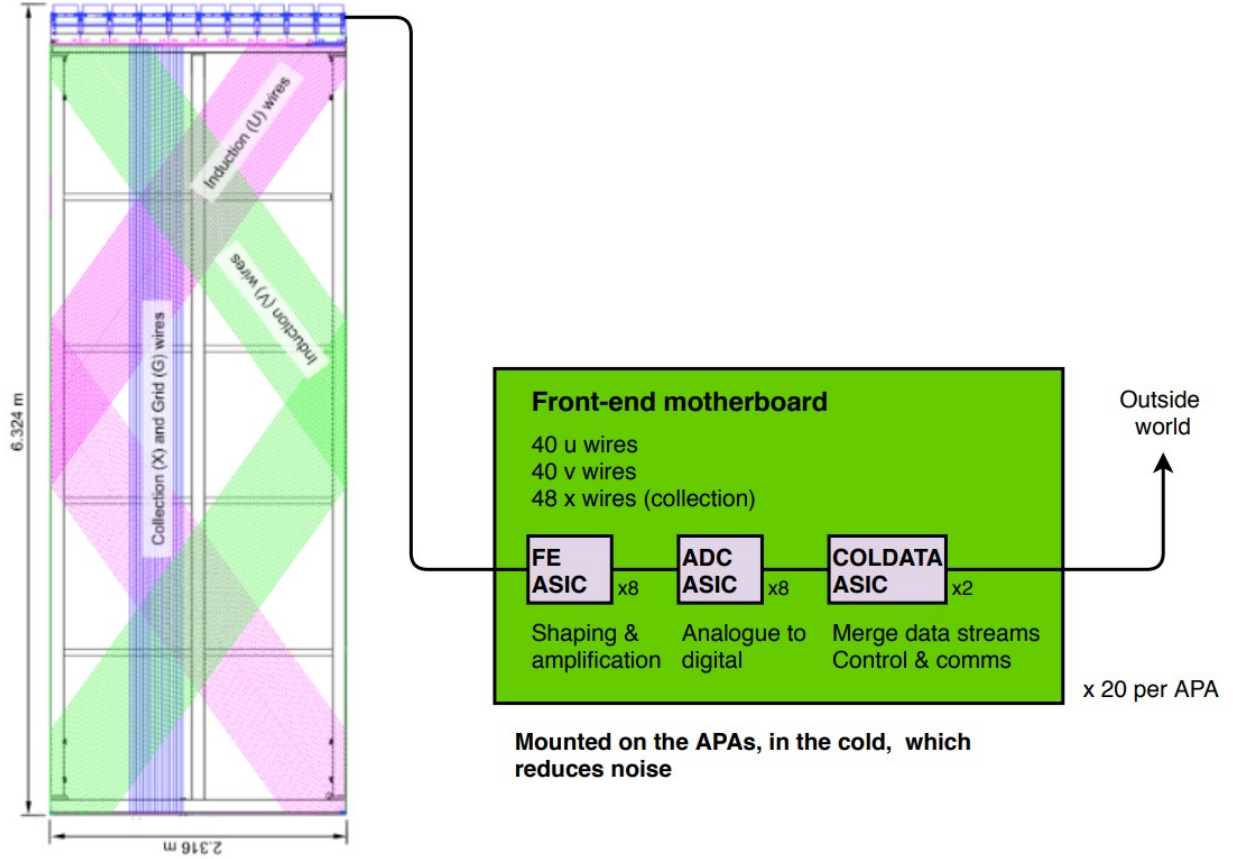
Figure 2.6: Image taken from [70], Fig 1.12 of section 1.8. Image shows an overlay the the relevant charge collection wires within a SP DUNE LArTPC.

discussed in section 2.1, we expect the looping of the 32-bit recorded value to not present a design concern.

The total number of free running oscillators (N_{osc}) per DUNE-APA for a given pixel pixel of 4 mm^2 is:

$$N_{osc} = \frac{915399}{16} \approx 57213 \tag{2.28}$$

N_{osc} represents the total number of front-end ASICs whose data must be aggregated and sent outside of the cold electronics to a warm interface. Therefore we expect the order of the number of free running oscillators per DUNE-APA $O(10^5)$. This also gives an order of magnitude estimate of the increase of number of ASICs compared to the MWPC readout of Single-Phase (SP) DUNE-FD.

Figure 2.2 shows that each APA uses 20 FEMBs to digitize 128 of the 2560 channels. Each FEMB
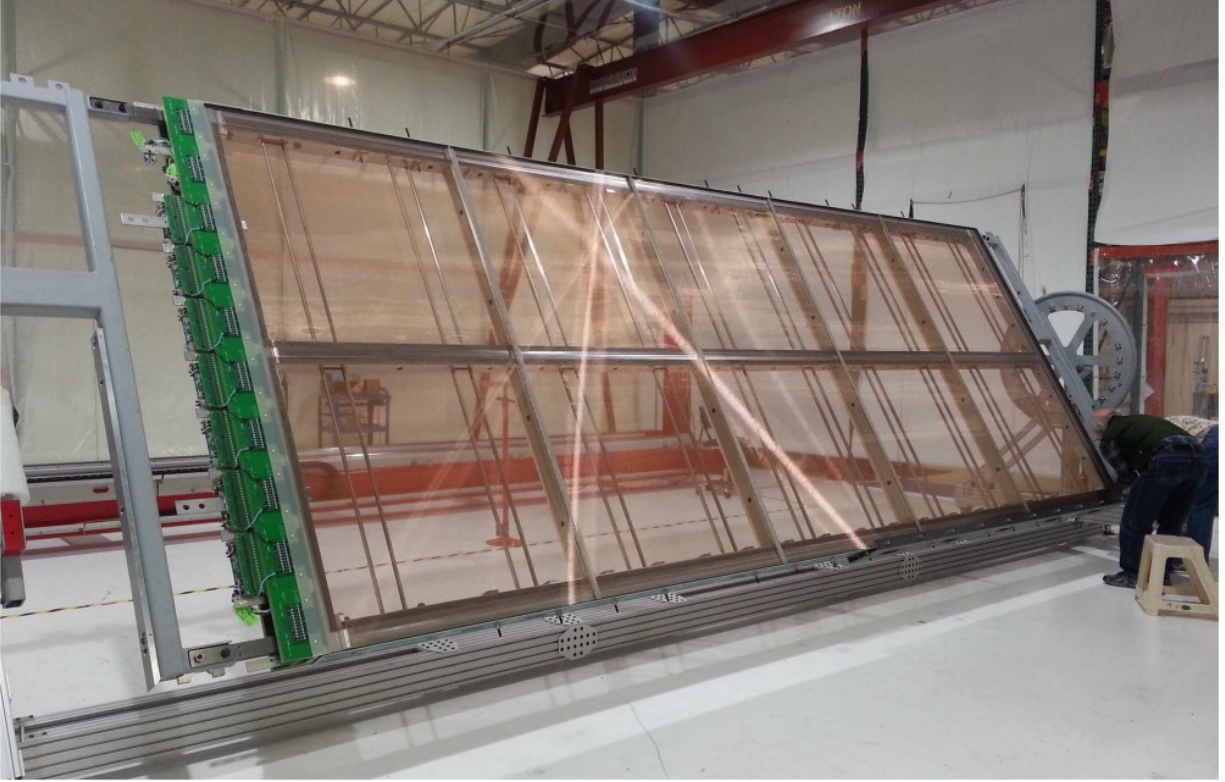
Figure 2.7: A simple caption [70]

houses a total of 18 ASICs which smooth, digitize, and aggregate data before being sent to the Warm Interface CRATE (WIC). The total number of ASICs per APA is $18 \times 20 = 360$. Since each 10 kt module uses 150 APAs the total number of ASICs would be multiplied by 150.

The goal of a digital backend design is how to handle the data from the 10^5 free running oscillators, and how to ensure that the free running local oscillator clocks can be calibrated to a known frequency. Additionally,

Single Point Failures

Here we comment on an overall design guideline for Q-Pix: "robust resilience" against single point failure (SPF). The readout technology presented here relies on huge numbers of readout channels (10^8) compared to current MWPC designs (10^5). As such, extra care must be made in designing new technology to improve over established, seemingly simpler means.

Description	Specification	Rationale
System Noise	< 1000 e^-	Provides >5:1 S/N on induction planes for pattern recognition and two-track separation.
Signal Saturation	500,000 e^-	Maintain calorimetric performance for multi-proton final state.
Cold Electronics Power Consumption	< 50 mW pre channel	No bubbles in LAr to reduce HV discharge risk
Number of Channels per front-end motherboard	128	The total number of wires on one side of an APA, 1,280, must be an integer multiple of the number of channels on the FEMBs.
Maximum diameter of conduit enclosing the cold cables while they are routed through the APA frame.	6.35 cm (2.5")	Avoid the need for further changes to the APA frame and for routing the cables along the cryostat walls

Table 2.1: Selected Requirements of DUNE TPC electronics and Expected QPix Design goals of first generation ASIC development for comparison. TPC electronic data and rationale are taken from [70]

This principal guides design choices such as the use of independent local oscillators at the pixel-level instead of a provided distributed clock. This design choice, in particular, is discussed at length in chapter 4, and the findings presented there are one of the major contributions presented in this work.

The design which avoids SPF and handles the digital requirements presented here, namely: the continual time calibration of each local oscillator ($N_{osc} \approx 10^5$) is a goal of this work.

2.4   Q-Pix and Light Detection

Other recent progress [75] has been made towards inclusion of an optical system combined the readout technology presented here. Such a system would integrate well with a charge-integrate-reset style presented here, as the charge collection area is much smaller than the total pixel area. The pixel dimensions are 4 mm × 4 mm for a total active area of 16mm^2. Most of this active area is unused for the charge collection pad, which could be as small as drill-hole via (6 mil << 16mm^2).

Description	Specification	Rationale
System Noise	$\approx 300e^-$	Provides $\approx$ 17:1 S/N ratio, a component of front-end integrator.
Signal Saturation	>30nA?	Upper limit from local oscillator frequency and integrator reset.
Cold Electronics Power Consumption	$< 100\mu$W per channel	Equivalent power consumption for heating
Number of Channels per Tile	??	Design parameter to be calculated.
Maximum diameter of conduit enclosing the cold cables while they are routed through the APA frame.	6.35 cm (2.5")	Same as [70], an engineering goal is to aim to use existing APA frame designs.

Table 2.2: Q-Pix based Requirements, which can be compared against 2.3. Results here are necessarily speculative, but provide a design goal baseline.

Then, most of the remaining area could be plated with a photo-sensitive material.

Such a photosensitive material could capture incoming scintillation photons and provide an additional voltage measurement at each pixel. Depending on the sensitivity, such a measurement could be used to reconstruct tracks by providing a $\frac{dE}{dX}$ measurement, or even as a time-tag and a trigger.

The use of a reference trigger could be useful to establish event-time within the same system, and allow adjacent pixels which would receive photons, but not charge, to contribute to time reconstruction. Any reconstructed event requires some T_o time to indicate the start of the event. Typically this is done via scintillation photons from a secondary system, where the photons arrive nearly instantly at the collection planes compared to the slow drift speed of the electrons.

The natural pixelization of QPix required the charge collection can also be used to be sensitive to scintillation photons. These photons could not only provide the required timing but also provide an additional means of calorimetry, and track reconstruction. Additional work is currently underway to demonstrate the viability.

Chapter 3

THE Q-PIX BACK-END AND SIMULATION STUDIES FOR FUTURE Q-PIX PROTOTYPES

This chapter highlights the requirements of a digital back-end suited to a Q-Pix based readout implemented in a LArTPC design.

The first part of this chapter details the design problem which must solve data collection rates, total data aggretation, and hardware constraints for a successful deployment. The Q-Pix readout (Chapter 2) relies on several key factors which promise possible improvements over a traditional MWPC readout: automatic calibration from quesicent background, an overall reduction in data collection, and simpler analysis and data reconstruction, to name a few. However, this novel readout technique not only changes the front-end analog structure but also dramatically increases the number of digitization channels. The increase of the number digital channels and required ASICs creates the need for a new digital-backend design.

The second part of this chapter describes a simulation framework which aims to parameterize the search for an optimal digital design. We use this simulation framework to address these questions, since any sufficiently complicated design offers an intractible number of possible choices which can signficantly alter the performance (good or bad) of a detector. The Q-Pix readout is no different. A few examples of crucial design choices for the digital back-end are: the use of free-running local oscillators, the selection of an inter-ASIC communication protocol, the choice of inter-ASIC connections or routing profiles, and the buffer sizes of FIFOs to store charge-reset data. The goal of the simulation is to parameterize these design choices.

The final part of this chapter summarizes the results of the simulations and provides, to the best of its ability, a description of the effects of the most important parameters determined from these results. We use as inputs to the simulation the expected input charge from radiogenic background and beamline neutrino interaction over a DUNE-FD APA. The characterization of the analog front-end, namely the charge characteristics per channel is an on-going collaborative work, whose results (when available) should be able to be applied here. The goal of the next chapter **??** is to provide a hardware verification of the simulation results presented here.

The vast majority of the work presented in this chapter is my own individual work.

3.1 The Digital Back-end problem

The main objectives of the digital back-end are to correctly measure the data presented to it by the analog front-end and ensure lossless transport of that data to disk. More simply, the goals of the digital portion of the Q-Pix readout are to record and send data. We note that the successful completion of these two objectives to be goal of these simulation studies.

The Basic Datum

We begin with a discussion of the basic datum recorded and mention initial design choices at this interface. The structure of this datum motivates the buffer widths and depths required to store the data at the local ASIC level as well as the protocol used to transfer this data between ASICs and eventually out of the detector.

The minimum data which needs to be recorded are the time, the relative location of the digitizing ASIC within the detector, plus any channels which were responsible for this reset. Each of the number of bits assigned to recording these parameters are a design consideration. We choose the number of bits for the timestamp (N_T) to be 32, which prevents frequency wrap-around based on a fast clock frequency (Equation **??**). We choose as the number of bits to assign a location (N_{loc}) to be 8, which provides a maximum possible number of unique positions before aggregation to be 256. Next, since the number of pixels (required by analog front-end design) is 16 we choose this number as the number of bits to represent a "mask" ($N_{bits} = 16$). We need to record all of the channels during each reset since it is technically possible (even if less likely) for multiple analog channels to provide a reset within the same clock window.

We calculate the minimum number of bits per datum to be:

$$N_{bits} = N_T + N_{pix} + N_{loc} = 32 + 16 + 8 = 56 \tag{3.1}$$

Since buffer memory addresses and widths are normally characterized by powers of two, we can construct the basic datum size above the minimum number of bits provided by 3.1 to get $N_{datum} = 64$. The remaining bits are useful for constructing different types of packets to be used by the digital ASICs for additional uses such as register configuration or to provide packet identification.

Communication of the Datum

Reserved	Word type	Channel mask		XPos	YPos	Timestamp	Timestamp data
Reserved	Word type	W R D	ReqID	Q	XHops	YHops	XPos	YPos	Address	Data	Reg request
Reserved	Word type	0	ReqID	0	XPos	YPos	Address	Data	Reg response
Reserved	Word type	0	Full	Req ID	Evt num	XPos	YPos	Interrogation time	Evt end

0x1 -- Timestamp data
0x3 -- Reg request
0x4 -- Reg response
0x5 -- Event end
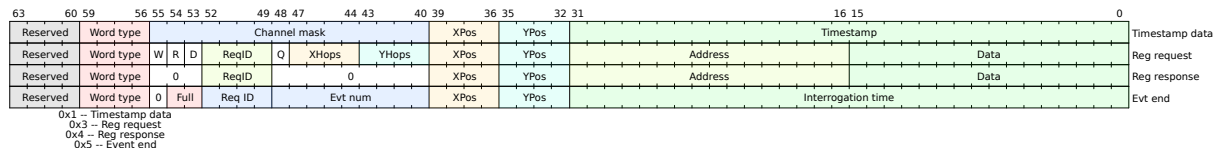
Figure 3.1: Example of Datum words and their allocation as currently implemented in the simulation and first prototypes.

There exist many asynchronous protocols of communication of digital information. Most of the differences between protocols exist based on the number of connections between devices and whether or not one pin is allocated to share a clock, etc.

Our design considerations for this readout include reduction of SPF risk, low power, and minimal routing. Partly for these reasons, the design choice for communication relies on only two connections between ASICs. One connection is defined as a data receiver (Rx) and the other as a data transmitter (Tx). This choice of interface dramatically limits a choice of possible protocols. Here, we describe the difference between two that we tested: Universal Asynchronous Receiver-Transmitter (UART) and Endeavor. We discuss and test only these two protocols for simplicity, and find it instructive to compare a proven and custom protocol (Endeavor) with a very common one (UART).

The importance of choosing a correct protocol is to ensure lossless data transmission. Since there are free running clocks, an asynchronous communication protocol is required. The way to ensure that data can be moved between clocks of different speeds is to stretch the signal or to repeat bits. The more the word is stretched in time, the larger the allowable difference in frequency between the two devices. However, this lengthening can't proceed forever, obviously, otherwise data transmission time could exceed data capture rates.

It is another important design consideration, then, to ensure that transactions proceed as quickly as possibly without data loss. Additional concerns of long data transactions include the use of more clock cycles which use more power and increase the risk noise to leak to the analog front-end.

UART

This common protocol is typically stable between devices with a maximum difference of clock frequency to be 10%.
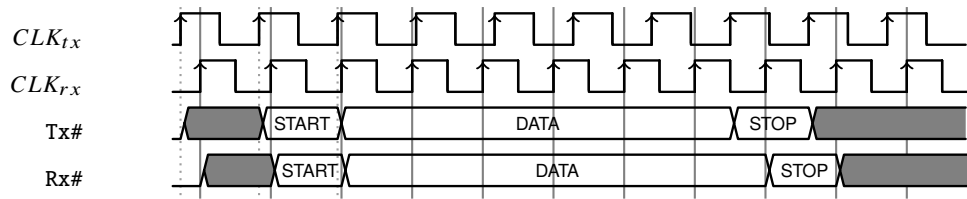
Endeavor

This protocol is slower than UART, but allows for approximately double the frequency difference: $\approx 20\%$.

The endeavor protocol relies on repeating the value of a high-bit, (digital '1' value) for an integer number of clock cycles. The receiver continually samples in incoming data transmission and counts the number of clock cycles that the signal was high for. The longer the signal was high, the more likely it is the the transmitter was attempting to encode a high bit, and vice verse.

The number of clock cycles which accompany either a high bit transmission or a low bit transmission then represent a possible design choice for the protocol. The actual number of bits which should be used ultimately depend on the similarity of the frequency between adjacent digital channels; the more similar the frequency (and relative phase) the lower these numbers can be.

- Start Bit

- High Bit

- Low Bit Send

- Stop Bit Send

3.2 Constraining the Digital-Backend Design

Section 2.2 describes in detail how a Q-Pix based hardware readout architecture could fit within a single DUNE-APA. Here we extend this discussion and use those constraints as the starting point for a search for a solution to the digital back-end architecture. The first problem to solve is how to aggregate the all timestamp data supplied by the large number of channels within a DUNE-FD APA.

A Q-Pix architecture would likely use either a high-performance FPGA or a custom ASIC to aggregate the large number of ($O(10^7)$) channels. The number of aggregated digital channels determines the required capabilities of the aggregator node and the selection of an FPGA or ASIC. Since each additional aggregator node represents an additional SPF risk, our design goal suggests that the optimal configuration is one that produces the least number of aggregator nodes. Therefore, the goal is to design a routing architecture which is responsible for as many digital channels as possible for each data aggregator node which still allows for accurate timing calibration and lossless data acquisition.

However, as one increases the number of digital channels per aggregator node one also increases the amount of local oscillators per aggregator, each of which must be calibrated. Additionally, since each digital channel requires extra communication time (as discussed in section 3.1) the introduction of more channels negatively affects the precision of timing calibrations and potentially increases SPF risk of digital channels. We consider then that an optimal number of digital channels per aggregator node is one that maximizes the number of digital channels but still maintains the required timing calibration (Sec. **??**) and transmits lossless data.

We refer to the total number of digital channels collected from one pathway to an aggregator as a tile. In a fully realized design an aggregator might in fact be responsible for multiple tiles, which need not necessarily be the same size. The requirements of an aggregator node is completely determined by the composition of tiles it is connected to. Then, a parameteriziation of the data requirements imposed by each tile can be extended to describe the requirements of the aggregator node. Finally, we reach the conclusion that the required parameterization of the back-end system relies on the parameterization of the tile.

A tile is composed of inter-connections between digital channels. The LArTPC design suggests that each digital channel have a maximum of four connections since the collection of charge happens on a flat two-dimmensional anode plane. Therefore, a two-dimensional routing requires at least two independent communication channels, which if we require the digital channels to allow bi-directional communication, the minimum number of channels is four. We use this number as a starting point for the digital channel design. These four connections per channel immediately creates a rectangular connection structure for a tile.

We note here that in order to meet other physical design requirements to fit into a pre-existing APA frame, the capability of the aggregator nodes could be increased to be responsible for more tiles, which would reduce the cable and hardware engineering considerations. However, further consideration here is beyond the scope of this work.

Tile Routing Considerations

A tile is a rectangular composition of digital channels which must provide a path to all digital channels and send lossless data to the aggregator. Since there is one connection between a tile and the aggregator, there is one special node within the tile that connects to the aggregator. This special node we refer to as the "base-node" as all data and instruction commands, regardless of routing, must pass through this node. The symmetry of the rectangular tile allows any corner node to be the base node, and we choose the upper-left to define a convention. An example of a tile with a Corner base-node is shown in Figure. 3.2.

We do not consider possible configurations where an aggregator might be connected to a digital channel within a tile since we require that all digtal channels are identical and fully connected. We require identical channels as a practical choice due the required number of total channels. We also require the tile to be fully connected to allow as many possible unique paths between the base-node and the other nodes which provides maximum protection against SPF. We address that we discuss why we do not consider base-nodes placed on the outer edge of a tile, but not at the corners more generally in section 3.2. Briefly, base-nodes which are along the outer edge of a FCT but not at the corners simply contain two sub-graphs of FCT with a base-node along the edge. Therefore, an analysis of the constraints of a FCT with corner base-nodes can be mapped to an analysis of FCT with edge base-nodes.

Here we introduce a particular representation (based on graph-theory) for a tile which is useful for simplifying simulations and for analyzing particular routing configurations. The most general tile configuration occurs when we assume that all adjacent nodes within the tile are connected; this creates what we refer to as a "fully connected tile" (FCT). An example of a FCT is shown in Figure **??**. Any particular choice of an effective routing must then be a subset of this fully connected version.

To elaborate on the adjacency matrix of the FCT we consider an 2×3 tile. A 2×3 tile has six total nodes, where we consider the upper-left most node to be the base node. Then, the unweighted
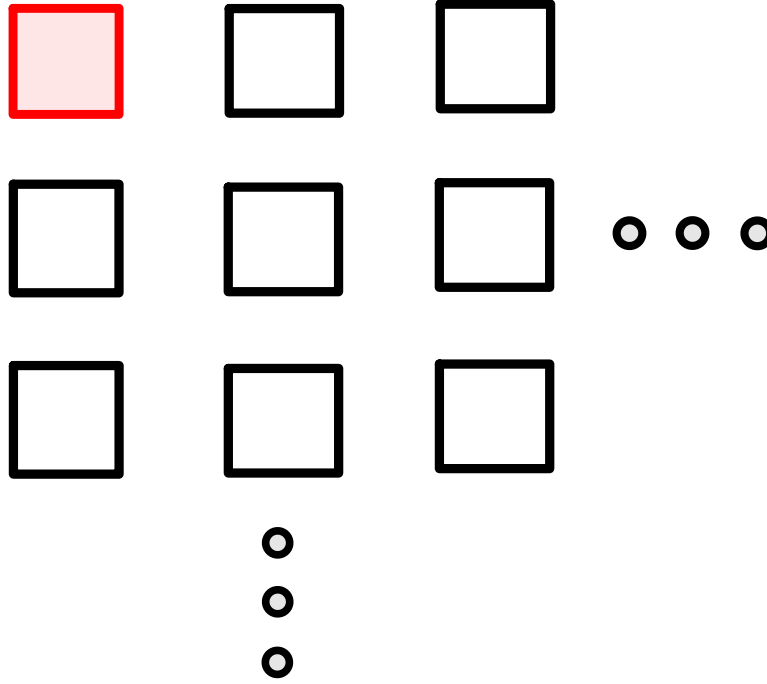
Figure 3.2: Example of an Corner Base-Node configuration. The base-node is colored and highlighted in red.

adjacency matrix has dimensions 6×6 of the form:

$$M = \begin{pmatrix} 0 & 1 & 0 & 1 & 0 & 0 \\ 1 & 0 & 1 & 0 & 1 & 0 \\ 0 & 1 & 0 & 0 & 0 & 1 \\ 1 & 0 & 0 & 0 & 1 & 0 \\ 0 & 1 & 0 & 1 & 0 & 1 \\ 0 & 0 & 1 & 0 & 1 & 0 \end{pmatrix} \tag{3.2}$$

Where each non-zero value of M_{ij} represents a connection between nodes i and j. As an unweighted, undirected graph this is a symmetric matrix.

In practice each digital channel within a tile is actually controlled by a unique, free-running oscillator. Therefore, we can define the length of each edge between nodes as the length of time to send of a packet of data between two nodes ($T_{i \to j}$). With this we can extend the model the adjacency matrix as a weighted and directed graph if we recognize that the non-zero elements of
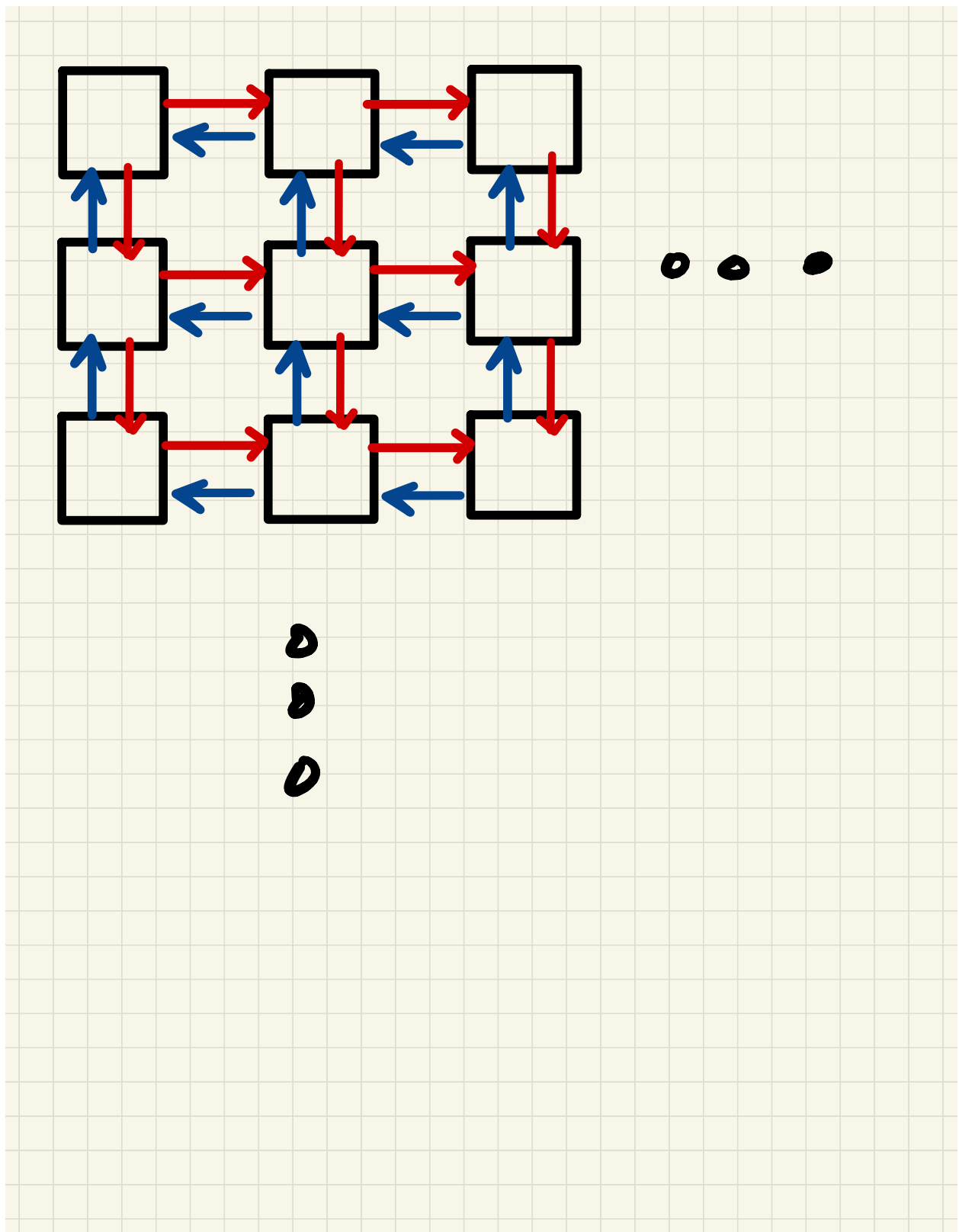
Figure 3.3: Example of the fully connected routing configuration for a tile (FCT). Each Node represents a digital channel which must be aggregated, and the red and blue connections distinguish directions of communication. The red connection lines indicate pathways away from the base node, whereas the blue lines represent connection paths towards the base-node in the upper-left.

M_{ij} become $T_{i\rightarrow j}$, or the length of time it takes for the ith local oscillator to transmit a packet to node j.

We can generalize this matrix in terms of an arbitrary number of rows (r) and columns (c). We define a convention of numbering nodes within the tile in terms of increasing column number followed by increasing row number. With this convention we obtain the general adjacency matrix with values defined by:

$$M_{ij} = T_{i\rightarrow j}(\delta_{i,j=i\pm 1} + \delta_{i,j=i\pm r}) \tag{3.3}$$

An adjacency list can similarly be constructed from Equation 3.2 where the non-zero connections are given by the kroniker-deltas factors.

The length between the nodes represets the time it takes for a packet to transact from one node to the next. This is determined by both the number of clocks to be sent in the communication protocol (N_{bits}) and the period of the transmitting and receiving oscillators, T_i and T_j, respectively. Unlike the transmitter, the receiver only affects the transaction time with a single clock cycle, as the protocls we test here, (UART and Endeavor), each conclude a packet transaction when the receiver records the last bit transaction from the transmitter.

The full length between two nodes, i and j, connected by an edge is represented by:

$$T_{i\rightarrow j} = N_{bits}T_i + T_j(t) \tag{3.4}$$

where $T_j(t)$ represents the time dependent fractional part of one nominal clock period of the receiving node. The expectation value of $T_j(t)$ is half of the nominal window so that mean Equation 3.2 is:

$$\bar{T}_{i\rightarrow j} \simeq N_{bits}T_i + \frac{T_j}{2} \tag{3.5}$$

Since the transaction time of a packet is much larger than a single clock cycle ($N_{bits} \simeq O(10^2) \gg \frac{1}{2}$), we can approximate Equation 3.2:

$$\bar{T}_{i\rightarrow j} \approx N_{bits}T_i \tag{3.6}$$

This representation is also useful to model certain SPF where a node becomes inactive. Dead or inactive nodes are ones in which all of their connections are effectively disconnected. This is equivalent to setting their transaction lengths to zero: $T_{SPF} = 0$.

We comment that although it is possible to construct tiles where more than one node connects to the aggregator, we observe that this configuration simply produces two effective tiles. These distinct tiles then are the data paths which are unique to each base-node. In this graphical representation a packet of data can follow one, and only one path from the origin node to the base-node unless there was duplication of packets. We emphatically avoid designs which might depend on data duplication for reduncancy; these two base-nodes are in unconnected graphs.

Additionally, it is possible to connect non-rectangular tiles, but these tiles are effectively a larger rectangular tile with disconnected nodes to produce the desired shape. Since every node is designed to be robust in the full version, it will be be robust in the subset.

We can apply this same argument to base-nodes which do not lie at the corners of the rectangular tile. In the case where the base-node is selected along the edge Therefore, we conclude that the analysis of the tile with the above adjacency matrix and a selection of the base-node at the corner of a rectangular corner provides the basis problem to the tile configuration.

The SPF Cost

We define the average SPF cost as the amount of nodes that will be lost during a transaction as the number of digital channels at a height below the failed digital channel. For example, the number of nodes which are lost if a leaf-node fails is one since no other channels are between it and the data node. Likewise, the number of nodes which are lost in the event of a base-node failure is the total tile, N.

We can then calculate a mean cost SPF, C_{SPF}, :

$$C_{SPF} = \frac{1}{N} \sum_{node} \frac{n_i}{N} = \frac{1}{N^2} \sum_{node} n_i \qquad (3.7)$$

Minimize Occupancy
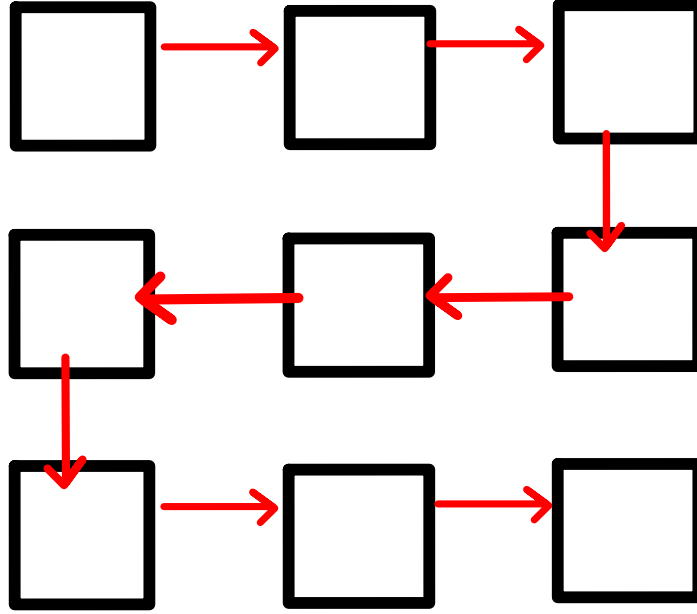
Figure 3.4: Minimal Occupancy Path of a FCT. This routing path ensures that the number of input connections equal the number of output paths for the node.

One of the goals of a succesful digital design is to ensure lossless data transfer. One point of failure on the digital side is an overabudance of data arriving at a single layer within the tree. This data loss occurs when data are sent to a node faster than the data leaves the node, and persists for long enough such that the buffers of the node overflow. This creates a horrible loss of data which can't be recovered.

A routing scheme which minimizes the overall occupancy in the tree depths is shown in Figure 3.2. We refer to the style of routing as "Snake"-routing (SR), because this is also the longest possible routing scheme for a square tile.

We inspect the SPF risk from this routing scheme with Equation 3.2, where we notice that the n_i of each node is simply a running sum from the leaf to N at the base node.

$$C_{SPF} = \frac{1}{N^2}\frac{N(N+1)}{2} = \frac{1}{n}\frac{N+1}{2} = \frac{1}{2} + \frac{1}{2N} \tag{3.8}$$

Equation 3.2 tells us that the SPF risk of this routing configuration converges to half as the size of the tile grows. Intuitively, this makes sense, since it is equally likely to select a node close to the base-node as it is far away, which implies that the sum should converge to half the tile size for large N.

Although this routing scheme provides the most lax constraint on the requried buffers at each digital channel, it provides the longest average path between the base node. The longer the transaction delay between the base-node and other nodes increases the reconstruction time uncertainty. Therefore, a natural alternative routing scheme is one that minimizes the communication scheme.

Minimize Delay

For any given node in an edge FCT with location (R_i, C_i), the shortest path to the base-node is simply the sum of its coordinates: $R_i + C_i$. An example of such a routing configuration for a tile is shown in Figure 3.2.

We can calculate C_{SPF} for this routing configuration if we identify that there are a C number of rows which sum from one to $R - 1$. Likelise, the far-left column in Figure 3.2 shows that the number of rows, R, sum from one to C. We can rewrite the sum over all nodes in Equation 3.2 as:

$$\sum_{node} n_i = C \sum_{i=0}^{i=R-1} i + R \sum_{i=0}^{i=C} i \tag{3.9}$$

We simplify the running sum of each term in Equation 3.2:

$$\sum_{node} n_i = C \frac{R(R-1)}{2} + R \frac{C(C+1)}{2} = RC \left(\frac{R+C}{2} \right) \tag{3.10}$$

Using this result we obtain C_{SPF} by identifying $N = RC$:

$$C_{SPF} = \frac{1}{N^2} \sum_{node} n_i = \boxed{\frac{R+C}{2RC}} \tag{3.11}$$

51
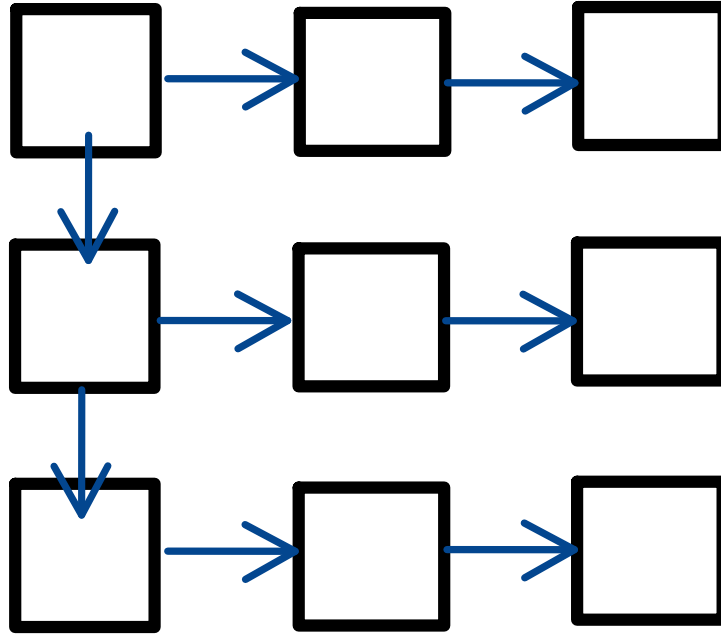
Figure 3.5: Minimal Delay Path of a FCT. This routing path ensures that the minimum number of transactions occur from every node in the FCT to reach the base-node. For any node along any column this is equivalent to the sum of the row and column of that node.

This result informs that relative cost of losing a node tends to zero as the size of the tile grows. Again, this result can be obtained intuitively, since as the number of columns (or rows) grow in size, the probability of a single failure occuring on the aggregator column is increasingly less likely.

Broadcasts to avoid SPF

In order to protect against SPF we only consider a designs which implement the FCT, since SPF can occur on any node the most robust connection scheme is the FCT. A FCT allows searches to probe all possible paths to any node via a "broadcast" produced from packets sent by the aggregator to the base-node. Therefore the broadcast algorithm can be represented by a complete circuit which begins at the base-node and proceeds to a target node with no repeated nodes until the target node

is reached. The backward path is then completed in reverse by following the edges (connections) between each node until arriving finally again at the base-node.

In practice, we encode the broadcast packet with a special header, to separate it from a request packet, and include an identification number. Then, any node which receives a broadcast packet will record the identification number of the most recent broadcast, which it can use to discard additional broadcast packets that arrive with the same number.

In the event that a particular node becomes inactive it will "block" data comming from the nodes along its path. In this case, there must be some sort of "broadcast" originating from the base-node that would allow information tranverse regardless of the effective routing path.

$$
\begin{pmatrix}
0 & 1 & 0 & 1 & 0 & 0 \\
1 & 0 & 1 & 0 & 1 & 0 \\
0 & 1 & 0 & 0 & 0 & 1 \\
1 & 0 & 0 & 0 & 1 & 0 \\
0 & 1 & 0 & 1 & 0 & 1 \\
0 & 0 & 1 & 0 & 1 & 0
\end{pmatrix}
$$
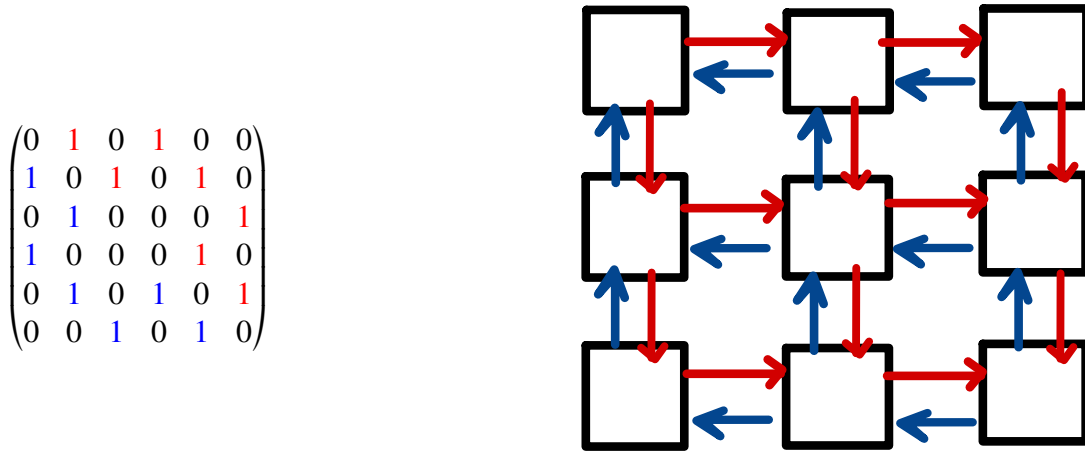
Figure 3.6: Minimal Routing Path of a FCT. This routing path ensures that the number of input connections equal the number of output paths for the node.

Comments on the Edge Base-node and Other Routings

We discuss here the case of a FCT with an edge base node. An edge base node (EBN) is a digital channel that connects to the aggregator and to three other digital channels within a tile. Like before, this base-node must provide a unique path during data transmission to all digital channels within the tile. In this configuration the adjacency matrix is still the same as given in Equation 3.2.

Also, as before, we wish to inspect different routing scenarios for a tile of a given square dimension
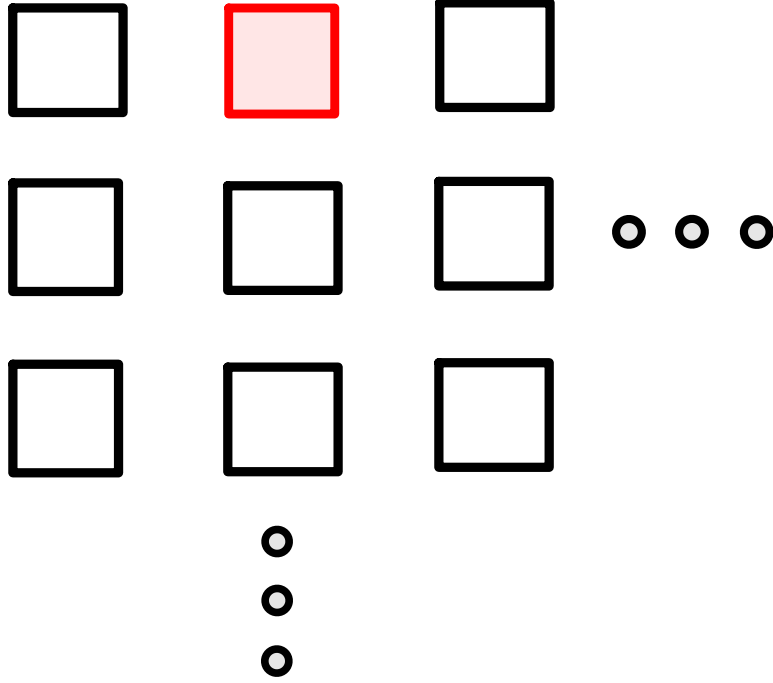
Figure 3.7: Example of an Edge base-node configuration. The base-node is colored and highlighted in red.

of R rows and C columns. We can proceed by dividing the FCT graph into two subgraphs, $S1$ and $S2$, where $S1$ represets the rectangular section of the graph below and to the left of the EBN, while $S2$ are the remaining channels.

We identify that while the number of columns (C) in tile is equal to both subgraphs, the total number of rows R of the tile is equal to the sum of the rows from these two subgraphs: $R = R_1 + R_2$.
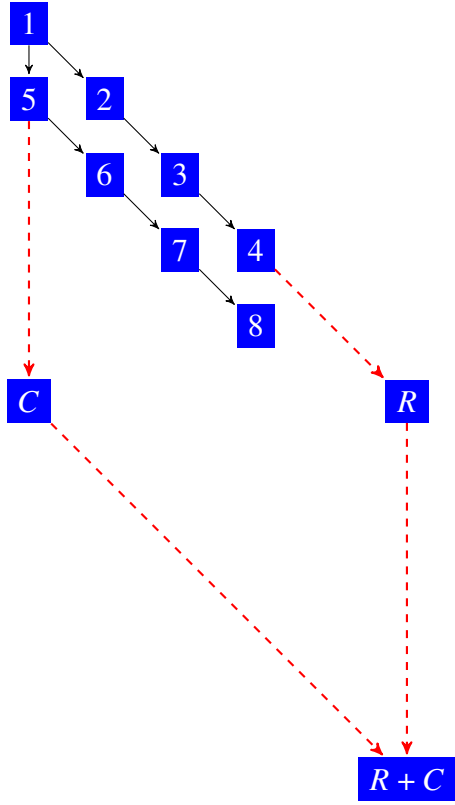
The EBN then is actually just a composition of two subgraphs which are each equivalent to The tree characteristics which determine requirements for the digital channels are the tree height and total occupancy at each level. Therefore, since the EBN provides no difference in either of these characteristics and is a suposition of two fundamental CBN, an analysis of an EBN is equivalent to the analysis of a CBN.

However, we do remark comment that the average difference of the relative weights of each node in a SPF analysis are different in a EBN compared to the CBN case. This should be obvious since the relative weight of each node is determined by the running sum of the path length betwee the base-node and its leaf. For a fixed row dimension, R, the EBN offers a smaller average tree height for each of its componet radia R_1 and R_2.

Therefore, in a EBN tile, with two subgraphs of radii R_1 and R_2 where the base-node is on the R_1 edge. The total sum of the weights of all nodes in the tile are the sums of the two subgraphs plus CR_2, which is the average weight of the nodes from the subgraph R_2 when it connects to R_1.

$$\sum_{node} n_i = \sum_{R_1} + \sum_{R_2} + CR_2 \tag{3.12}$$

Equation 3.2 gives the general formula for calculating the SPF risk for a EBN case, depending on the routing methods of subgraphs R_1 and R_2. We can treat these sub-graphs as in equation 3.2 to obtain:

$$\sum_{R_1} + \sum_{R_2} + CR_2 = \frac{R_1C(R_1+C)}{2} + \frac{R_2C(R_2+C)}{2} + CR_2 \tag{3.13}$$

We use this result to obtain the relation of the general C_{SPF}:

$$C_{SPF} = \frac{1}{N^2}\left(\frac{R_1C(R_1+C)}{2} + \frac{R_2C(R_2+C)}{2} + CR_2\right) \tag{3.14}$$

if we identify that $N = C(R_1 + R_2)$ and use $R_2 = R - R_1$:

$$C_{SPF} = \frac{1}{2CR^2}\left(2R_1^2 - 2R_1R + R^2 + CR + 2(R - R_1)\right) \tag{3.15}$$

3.3   Frequency Calibration of Local Oscillators

The Q-Pix calibration requirements are described in detail in Section 2.1. The important parameters which must be calibrated for each pixel are the charge per reset and the frequency of the local oscillator. An aim of this work is to demonstrate an additional frequency calibration method using the minimal required connections between each digital node.

Any method of a frequency calibration must synchronize time measurements between all digital nodes within a tile and the aggregator. There are several possibile methods to achieve this, but ultimately the data that are recorded must be some time at the aggregator, T_a, and the time at any specific node, T_j.

A direct method is one where the aggregator distributes its own clock to all nodes in the tile. This scenario removes the need for a calculation of the frequency of each node altogether since the clock of each node is already known from the aggregator. This is the simplest case for timing calibration: remove all free running oscillators. However, this method also introduces complex routing and power requirements within every tile.

A distributed clock network indeed removes ambiguity of the remote oscillator frequencies, but at the cost of hardware complexity. Whether or not this design choice is preferred is entirely detector dependent, but likely increases in difficulty with the scale of the TPC.

We comment, however, that we ignore this scenario because it may altogether be unnecessary depending on future ASIC performance. In the event that frequency calibrations of sufficient

precision ($\bar{f} \approx 1ppm$) are possible occur on free-running local oscillators future detectors would need only to acquire these ASICs and place them with minimal cost in terms of both time and money.

Another simple scenario is one where the aggregator itself connects directly to all nodes within a tile via a single connection which can be used as a reference trigger. This means that some trigger from the aggregator would issue directly into each node at the same time: $T_a = T_n$. To calcuate the frequency in this manner, the controller would issue two triggers from the aggregator with a known time separation, $T_o = T_{a2} - T_{a1}$. The remote nodes would each record and send their timestamps back to the aggregator, where the time difference would be calculated as:

$$T_o = T_{a2} - T_{a1} = T_{n2} - T_{n1} \tag{3.16}$$

this is rewritten in terms of frequency as follows:

$$f_n = \frac{T_{n2} - T_{n1}}{T_o} \tag{3.17}$$

This calibration method extremely simple but introduces an additional connection to each node between itself and the aggregator. For a large scale system such as Q-Pix even this simple connection scheme introduces $\approx 60 \times 10^3$ hardware points of failure per APA.

Both of these scenarios are valid implementations of a Q-Pix readout system. In both of these scenarios, however, there is added complexity into the hardware design of the system in the form of additional routing where each route which represents a possible point of failure.

In a world of perfect hardware and costless routing in terms of both time and money these routing schemes would clearly be sufficient. However, no hardware is perfect. Therefore we introduce and discuss a calibration technique which relies on no additional routing and could be optionally implemented even in the above schemes in the event of a failure. Therefore, even if not the primary implemented calibration technqiue, since this calibration introduces no superfluous routing it could still be used regardless of the actual future hardware implementation.

A Minimal Connection Calibration Procedure

As stated in the previous section, any frequency calibration records a reference time at the aggregator (T_a) and an event time (T_n) at a node within a tile.

the time calibration procedure presented here requires only the minimal routing required in any Q-Pix readout system, where we assume time-dependent free-running local oscillators at each node within the tile.

The calibration procedure begins at a time (T_0) where the aggregator sends a calibration packet.

Next, the packet propagates through the tile to some remote node, N_j. This node receives the packet later at some time T_{n1}:

$$T_{n1} = T_o + T_{f1} \tag{3.18}$$

Where T_{f1} is the propogation time of the packet from the aggregator to the N_j node.

This remote node then sends the packet with its time (T_{n1}) back to the aggregator.

The aggregator will wait some calibration time (T_{cal}) before issuing another calibration packet. This wait period $(O(10^{0-2}))$ can be long compared to the full transaction time to the N_j node $(O(j * 10^{-5}))$.

After the wait period, the aggregator will issue a second calibration packet to be sent to a remote node at time:

$$T_1 = T_{cal} + T_0 \tag{3.19}$$

Similarly to the first packet this packet will propagate to N_j with some new time T_{f2} where N_j will record time T_{n2}:

$$T_{n2} = T_1 + T_{f2} \tag{3.20}$$

Now, we define ΔT_j as the difference in the two time measurements from the two packets sent from the aggregator. The time difference is related to the number of clocks that occured between the two different measured values of the clock, T_{n1} and T_{n2}.

$$\Delta T_j = T_{n2} - T_{n1} \tag{3.21}$$

We use the known relationships for T_{n2} and T_{n1} to obtain:

$$\Delta T_j = (T_1 + T_{f2}) - (T_o + T_{f1}) = (T_1 - T_0) + (T_{f2} - T_{f1}) = T_{cal} + \Delta T_f \tag{3.22}$$

Where we defined ΔT_f as the difference in forward propagation times from the packets sent from the aggregator node at T_1 and T_0.

We arrive at the result which compares the measured time at the aggregator T_{cal} and the time measured at each node, ΔT_j:

$$\Delta T_j = T_{cal} + \Delta T_f \qquad (3.23)$$

A perfect reconstruction of the nodal frequency would follow if $\Delta T_f = 0$. But it is sufficient to note that the wait period happens on the order of seconds, whereas ΔT_f is on the order of μs or at least a six order of magnitude difference. We then use $\Delta T_f \ll T_{cal}$ to obtain:

$$\Delta T_j \approx T_{cal} \qquad (3.24)$$

We convert time into frequency with the difference of the timestamps measured and a known aggregator frequency (f_a):

$$\frac{\Delta N_j}{f_j} = \frac{\Delta N_a}{f_a} \qquad (3.25)$$

or,

$$\boxed{f_j = \frac{\Delta N_j}{\Delta N_a} f_a} \qquad (3.26)$$

Where ΔN_j and ΔN_a are the differences in the timestamps of the 32-bit clocks at the remote node and aggregator, respectively.

Packet Transaction Time

We next examine the approximation that $\Delta T_f \ll T_{cal}$ and consider its contribution to the error in the reconstruction of T_j. This analysis also provides a constraint on the duration of T_{cal} to ensure an accurate measurement of each T_j in a tile. We begin by discussing how long it takes for a packet to traverse a tile.

The time it takes for each packet to be received by the next node is given in Equation 3.2. The value, N_{bit}, is the number of clock cycles used for the packet and is protocol-dependent. Since the protocol must be deterministic for each packet, N_{bits} must be the same for each transaction on the path from the base-node to the remote node.

As an example, the time it takes for a packet to go from the base-node, N_1, to a remote node, N_3, via the path $1 \rightarrow 2 \rightarrow 3$ is determined by:

$$T_{1\rightarrow3} = T_{1\rightarrow2} + T_{2\rightarrow3} \approx \frac{N_{bits}}{f_1} + \frac{N_{bits}}{f_2} = N_{bits}\left(\frac{1}{f_1} + \frac{1}{f_2}\right) \qquad (3.27)$$

Where, f_i, is the frequency of the clock at sending node. The approximation is within a single clock cycle of the receiving digital node (≈ 33 ns).

Therefore the time it takes for a packet for go from the base-node to any remote node is proportional to N_{bits} multiplied by the sum of the edges in the full adjacency matrix given by Equation 3.2.

We generalize Equation 3.3 to represent the time it takes a packet to go from the aggregator ($i = 0$) to any remote node, N_j:

$$T_f = T_{0 \to j} = N_{bits} \sum_{i=0}^{i=j-1} \frac{1}{f_i} \tag{3.28}$$

We require that every calibration packet on the protocol uses the same number of clocks (N_{bits} is constant) and follows the same path. ΔT_f becomes:

$$\Delta T_f = N_{bits} \sum_{i=0}^{i=j-1} \frac{1}{\Delta f_i} = N_{bits} \sum_{i=0}^{i=j-1} \Delta T_i \tag{3.29}$$

We recognize ΔT_i as the nominal time-dependent clock drift of the each local oscillator in the path between the base-node to the remote-node. We can provide an order of magnitude estimate for ΔT_f if we assume a (very poor) $\approx 1\%$ drift in each of the remote clocks within the tile during a period of $T_{cal} \approx 1$ s. In this approximation we also assume that the mean of the periods of the nodes are the designed value (≈ 33 ns) for which a 1% error gives $\sigma_{T_f} \approx 3$ ps. If we assume that all of the clocks (for whatever reason) drift have error which drifts int he same direction (the sum doesn't cancel) then for 100 transactions with 1000 clocks per transaction, we obtain for ΔT_f:

$$\Delta T_f \approx 1000 * 100 * 3 \times 10^{-12} \approx 30 \text{ ns} \ll 1 \text{ s} \simeq T_{cal} \tag{3.30}$$

3.4 Physical Simulation Studies

We now discuss the implementation of the simulation based on the previous sections.

Simulated Detector Properties

3.5 Radiogenic Backgrounds as a Calibration Source

sources of backgrounds are taken from [70]

3.6 Supernova Studies

Work has been done to understand how a Q-Pix based DUNE-FD would measure core collapse supernovae [76].

Simulation studies which involved particle interactions were based on Geant4 [77].

3.7 Neutrino Beam High Energy Studies

3.8 Summary and Further Studies

C h a p t e r 4

DIGITAL BACK-END VIABILITY STUDIES

In this chapter we describe the overall structure digital back-end of the Q-Pix design. We would like to take a moment here to note here that we refer to each node in the array is implemented as a lattice ice40UP FPGA

Additionally, this chapter is divided into two parts. The first part we give a detailed description of the digital-system, and its requirements to successful in a Q-Pix based detector of DUNE scales. The motivation here is to outline how the digital backend of Q-Pix based readout fits into the DUNE-FD LArTPC. The second part of this chapter is dedicated to the first evaluation boards developed and tested which are implemented in Lattice iCE40UP FGPAs [78]. The second part outlines the design of the PCB on which these FPGAs are implemented, as well as basic results of these FGPAs, which are motivated from the first part of this chapter.

The Lattice Semiconductor FPGAs [78] were selected because of the small form factor, pin out, availability, as well as lower power consumption. There are planned tests for future, but not presented here to indicate its viability of over-the-counter FPGAs in LArTPc. If such cheap and available FPGAs were shown to be reliable use in a LArTPC environment, that would greatly influence future detector development and selection for Q-Pix.

The vast majority of the work presented in this chapter is my own individual work.

4.1 Digital Design Overview

The digital system of the entire Q-Pix design begins at the electronic collection of a recorded timestamp in respond to a reset-time-difference sent from the analog front-end. Then, all data that are recorded for each pixel, and the only data required for a full analysis of all reconstruction with a LArTPC are:

- 32 bit timestamp

- Pixel X location ($\leq$ 4 bits)

- Pixel Y location ($\leq$ 4 bits)

- APA reference number ($\leq$ 4 bits)
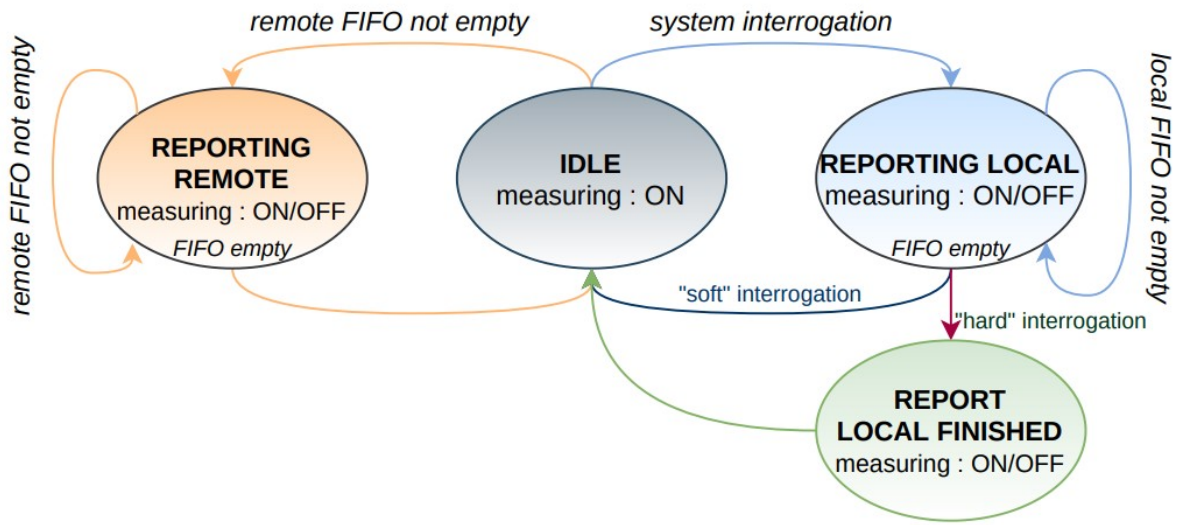
Figure 4.1: Diagram of the Digital node's FSM which determines how to respond to incoming packets.

Each of these remote ASICs are running on free-running independent clocks, with an expected frequency of $\approx$ 30 MHz.

Basic System Requirements

Reset time differences are a function of the accumulated charge compared to the integrating capacitance for this specific pixel. The sheer number of pixels required for an APA (and the entire module) require an effective means of charge and time calibration, stable buffer depths, and protection against single-point failure (SPF).

Charge Calibration of each Pixel

Natural decay products produced by ^{39}Ar provide a continous source of incoming current across a LArTPC.
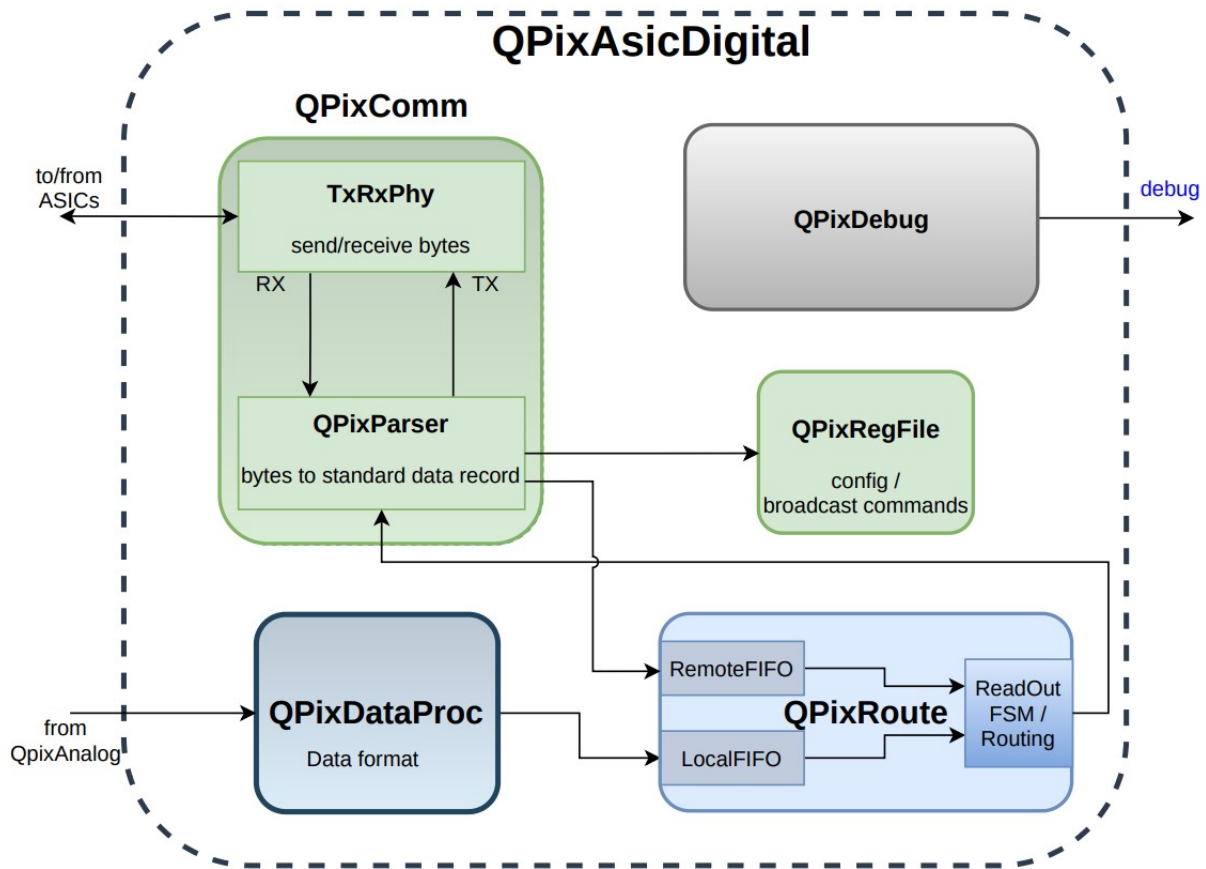
Figure 4.2: Diagram of the Digital node.

Time Calibration of each Node

Inter-Node communication via endeavor protocol

The Structure of a Data Word

Each node communicates via an entire packet, which is always 64 bits long. The communication protocol (4.1)

Comments on Data Rates and required Computing

Based on the minimum number of bits for each RTD 4.1 we can calculate minimum data rates for a full APA section and extend to this to
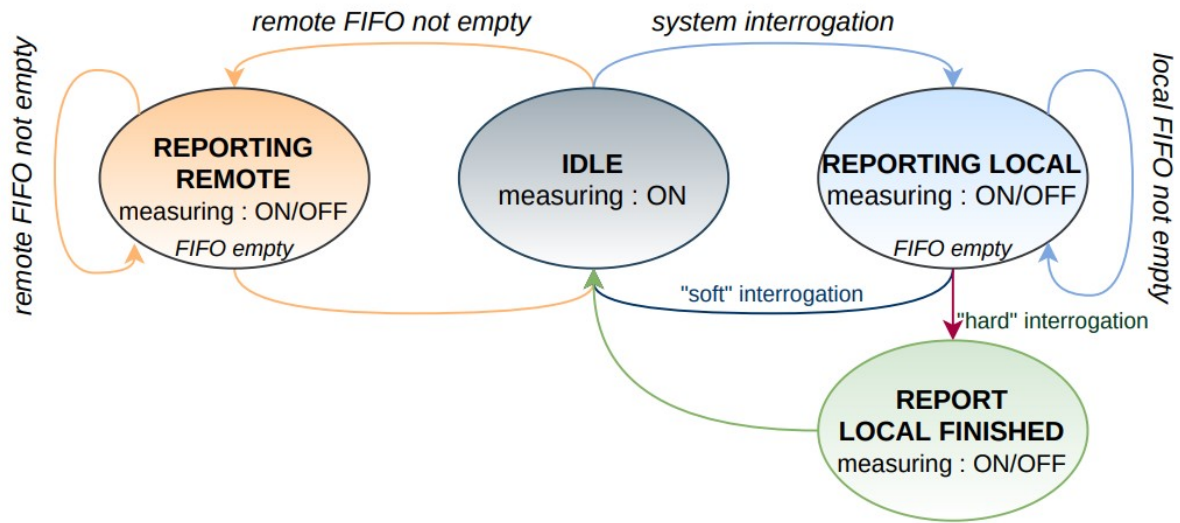
Figure 4.3: Overview of the FSM design, courtesy of Vasily Shebalin.

4.2 The Digital Finite State Machine

The Finite State Machine (FSM) of the remote digital ASIC outlines the designed behavior response to inputs from a controlling DAQ node.

- Idle, Acquisition State

- Transmit Local

- Transmit Finish

- Transmit Remote

- DONE

4.3 The Parameter Space of the Digital System

Buffer Depth Requirements

The required buffer depth of each node in an array is the maximum number of timestamps the node can store in memory before running out of room.

4.4   The Prototype Design

4.5   Power and Current Characteristics

4.6   Timing Stability

We describe here the methods of measuring a stable time for different configurations of the nodes. We also comment on the results of the timing with resepect to the minimum required timing sensitivity in order to have accurate timestamp reconstruction.

4.7   Analysis of Systematics for Different System Implementations

4.8   Towards the Integration of a DAQ-Node

4.9   Comments on A Super-DAQ-Node

Each APA module within a larger DUNE module must ultimately be interconnected so that the entire module can be readout. As described above, a single modular tile is controlled by an individual DAQ node, where many constitute a complete APA. Therefore, we refer to the device that digitally multiplexes all of the DAQ node data as the "Super DAQ Node" (SDN). Then, we imagine the final multiplexing stage for an entire DUNE module as an array of SDNs, each of which consistute an array of DAQ nodes, where each DAQ node is a 2-D array of Q-Pix based ASICs.

The total number of request SDNs within the full dune module depends on the final size of a DAQ-node controlled tile.

4.10   Summary

NEW DIFFUSION MEASUREMENTS: STUDIES WITHIN SAQ

In this chapter we introduce the first implementation of the Q-Pix based design using purely "over-the-counter" electronics.

5.1 Simplified Analog Q-Pix: System Design

5.2 The SAQ Protoype Design

5.3 Diffusion in Noble Gasses

Measurements of Transverse and Longitudinal diffusion of electrons within electric fields of strength 500 V/cm have been performed before [79].

5.4 Measurements of Leakage Current

5.5 The Diffusion background

5.6 Xenon Gas Lamp Measurements

Integrating towards background Current

5.7 Results and Discussion

Chapter 6

SUMMARY AND OUTLOOK

Recap of Qpix Requirements for DUNE APA here.

Recap of Qpix design concept testing within SAQ here.

Recap of QDB Results here

Recap of SAQ Results here

Recap of lessons learned on pixelated detectors

Discuss how combination of simulation / qdb / saq results motivate the next stage of development for QPix and incorporating the digital / analog ASICs for round two.

BIBLIOGRAPHY

[1] S. L. Glashow, "Partial-symmetries of weak interactions", Nuclear Physics **22**, 579–588 (1961).

[2] A. Salam and J. C. Ward, *Electromagnetic and weak interactions*, tech. rep. (IMPERIAL COLL OF SCIENCE and TECHNOLOGY LONDON (ENGLAND), 1964).

[3] S. Weinberg, "A model of leptons", Physical review letters **19**, 1264 (1967).

[4] R. L. Workman and Others, "Review of Particle Physics", PTEP **2022**, 083C01 (2022).

[5] D. Dominguez, *Cern accelerating science*, 2015.

[6] M. Gell-Mann, "The Eightfold Way: A Theory of strong interaction symmetry", 10.2172/4008239 (1961).

[7] M. Gell-Mann, "A schematic model of baryons and mesons", Physics Letters **8**, 214–215 (1964).

[8] J. J. Aubert, U. Becker, P. J. Biggs, J. Burger, M. Chen, G. Everhart, P. Goldhagen, J. Leong, T. McCorriston, T. G. Rhoades, M. Rohde, S. C. C. Ting, S. L. Wu, and Y. Y. Lee, "Experimental observation of a heavy particle J", Phys. Rev. Lett. **33**, 1404–1406 (1974).

[9] E. D. Bloom, D. H. Coward, H. Destaebler, J. Drees, G. Miller, L. W. Mo, R. E. Taylor, M. Breidenbach, J. I. Friedman, G. C. Hartmann, and H. W. Kendall, "High-Energy Inelastic e-p Scattering at 6° and 10°", prl **23**, 930–934 (1969).

[10] M. Breidenbach, J. I. Friedman, H. W. Kendall, E. D. Bloom, D. H. Coward, H. Destaebler, J. Drees, L. W. Mo, and R. E. Taylor, "Observed Behavior of Highly Inelastic Electron-Proton Scattering", prl **23**, 935–939 (1969).

[11] S. W. Herb et al., "Observation of a dimuon resonance at 9.5 gev in 400-gev proton-nucleus collisions", Phys. Rev. Lett. **39**, 252–255 (1977).

[12] S. Abachi et al., "Observation of the top quark", Physical Review Letters **74**, 2632–2637 (1995).

[13] S. H. Neddermeyer and C. D. Anderson, "Note on the nature of cosmic-ray particles", Phys. Rev. **51**, 884–886 (1937).

[14] M. L. Perl et al., "Evidence for anomalous lepton production in $e^+ - e^-$ annihilation", Phys. Rev. Lett. **35**, 1489–1492 (1975).

[15] K. Kodama et al., "Observation of tau neutrino interactions", Physics Letters B **504**, 218–224 (2001).

[16] R. Brandelik et al., "Evidence for planar events in e+e- annihilation at high energies", Physics Letters B **86**, 243–249 (1979).

[17] D. P. Barber et al., "Discovery of three jet events and a test of quantum chromodynamics at petra", Phys. Rev. Lett. **43**, 830–833 (1979).

[18] G. Arnison et al., "Experimental observation of isolated large transverse energy electrons with associated missing energy at s=540 gev", Physics Letters B **122**, 103–116 (1983).

[19] G. Arnison et al., "Experimental observation of lepton pairs of invariant mass around 95 gev/c2 at the cern sps collider", Physics Letters B **126**, 398–410 (1983).

[20] P. Higgs, "Broken symmetries, massless particles and gauge fields", Physics Letters **12**, 132–133 (1964).

[21] G. Aad et al., "Observation of a new particle in the search for the standard model higgs boson with the atlas detector at the lhc", Physics Letters B **716**, 1–29 (2012).

[22] J. L. Hewett et al., *Fundamental physics at the intensity frontier*, 2012.

[23] A. Airapetian et al., "ATLAS: Detector and physics performance technical design report. Volume 2", (1999).

[24] G. L. Bayatian et al., "CMS Physics: Technical Design Report Volume 1: Detector Performance and Software", (2006).

[25] T. Abe et al., *Belle ii technical design report*, 2010.

[26] "Juno physics and detector", Progress in Particle and Nuclear Physics **123**, 103927 (2022).

[27] D. A. Glaser, "Some effects of ionizing radiation on the formation of bubbles in liquids", Phys. Rev. **87**, 665–665 (1952).

[28] J. Chadwick, "The intensity distribution in the magnetic spectrum of beta particles from radium (B + C)", Verh. Phys. Gesell. **16**, 383–391 (1914).

[29] J. S. Chadwick, "Possible existence of a neutron", Nature **129**, 312–312 (1932).

[30] E. Fermi, "Versuch einer Theorie der β-Strahlen. I", Zeitschrift fur Physik **88**, 161–177 (1934).

[31] C. L. Cowan, F. Reines, F. B. Harrison, H. W. Kruse, and A. D. McGuire, "Detection of the free neutrino: a confirmation", Science **124**, 103–104 (1956).

[32] G. Danby, J.-M. Gaillard, K. Goulianos, L. M. Lederman, N. Mistry, M. Schwartz, and J. Steinberger, "Observation of high-energy neutrino reactions and the existence of two kinds of neutrinos", Phys. Rev. Lett. **9**, 36–44 (1962).

[33] F. P. An et al., "Observation of electron-antineutrino disappearance at daya bay", Phys. Rev. Lett. **108**, 171803 (2012).

[34] Q. R. Ahmad et al., "Direct evidence for neutrino flavor transformation from neutral-current interactions in the sudbury neutrino observatory", Phys. Rev. Lett. **89**, 011301 (2002).

[35] M. A. Acero et al., "First measurement of neutrino oscillation parameters using neutrinos and antineutrinos by nova", Phys. Rev. Lett. **123**, 151803 (2019).

[36] K. Abe et al., "Indication of electron neutrino appearance from an accelerator-produced off-axis muon neutrino beam", Phys. Rev. Lett. **107**, 041801 (2011).

[37] J. K. Ahn et al., "Observation of reactor electron antineutrinos disappearance in the reno experiment", Phys. Rev. Lett. **108**, 191802 (2012).

[38] S. Fukuda et al., "Determination of solar neutrino oscillation parameters using 1496 days of super-kamiokande-i data", Physics Letters B **539**, 179–187 (2002).

[39] K. Eguchi et al., "First results from kamland: evidence for reactor antineutrino disappearance", Phys. Rev. Lett. **90**, 021802 (2003).

[40] Y. Abe et al., "Indication of reactor $\overline{\nu}_e$ disappearance in the double chooz experiment", Phys. Rev. Lett. **108**, 131801 (2012).

[41] R. Davis, D. S. Harmer, and K. C. Hoffman, "Search for neutrinos from the sun", Phys. Rev. Lett. **20**, 1205–1209 (1968).

[42] G. Charpak, R. Bouclier, T. Bressani, J. Favier, and C. Zupancic, "The Use of Multiwire Proportional Counters to Select and Localize Charged Particles", Nucl. Instrum. Meth. **62**, 262–268 (1968).

[43] J. N. Marx and D. R. Nygren, "The time projection chamber", Physics Today **31**, 46–53 (1978).

[44] E. Aprile et al., "The XENON1t dark matter experiment", The European Physical Journal C **77**, 10.1140/epjc/s10052-017-5326-3 (2017).

[45] B. Abi et al., "Volume i. introduction to dune", Journal of Instrumentation **15**, T08008 (2020).

[46] C. Rubbia, *The liquid-argon time projection chamber: a new concept for neutrino detectors*, tech. rep. (1977).

[47] R. Acciarri et al., "Demonstration of mev-scale physics in liquid argon time projection chambers using argoneut", Phys. Rev. D **99**, 012002 (2019).

[48] R. Acciarri et al., "Design and construction of the microboone detector", Journal of Instrumentation **12**, P02017 (2017).

[49] R. Acciarri et al., "The liquid argon in a testbeam (lariat) experiment", Journal of Instrumentation **15**, P04026 (2020).

[50] A. Friedland and S. W. Li, "Understanding the energy resolution of liquid argon neutrino detectors", Phys. Rev. D **99**, 036009 (2019).

[51] *Liquid Argon Properties (Tables and Calculators) kernel description*, `https://lar.bnl.gov/properties/`, Accessed: 2023-01-04.

[52] F. Arneodo, *The icarus experiment, a second-generation proton decay experiment and neutrino observatory at the gran sasso laboratory*, 2001.

[53] K. Abe et al., "Search for proton decay via $p \rightarrow e^+\pi^0$ and $p \rightarrow \mu^+\pi^0$ in 0.31 megaton · years exposure of the super-kamiokande water cherenkov detector", Phys. Rev. D **95**, 012004 (2017).

[54] P. Nath and R. Arnowitt, "Limits on photino and squark masses from proton lifetime in supergravity models", Phys. Rev. D **38**, 1479–1484 (1988).

[55] H.-K. Proto-Collaboration et al., *Hyper-kamiokande design report*, 2018.

[56] G. M. Fuller, R. W. Mayle, J. R. Wilson, and D. N. Schramm, "Resonant Neutrino Oscillations and Stellar Collapse", apj **322**, 795 (1987).

[57] K. Abe et al., "Measurements of neutrino oscillation in appearance and disappearance channels by the t2k experiment with 6.6×10^{20} protons on target", Phys. Rev. D **91**, 072010 (2015).

[58] B. Pontecorvo, "Inverse beta processes and nonconservation of lepton charge", Zh. Eksp. Teor. Fiz. **34**, 247 (1957).

[59] Z. Maki, M. Nakagawa, and S. Sakata, "Remarks on the Unified Model of Elementary Particles", Progress of Theoretical Physics **28**, 870–880 (1962).

[60] X. Qian and P. Vogel, "Neutrino mass hierarchy", Progress in Particle and Nuclear Physics **83**, 1–30 (2015).

[61] L. Wolfenstein, "Neutrino oscillations in matter", Phys. Rev. D **17**, 2369–2374 (1978).

[62] A. Y. Smirnov, "The msw effect and matter effects in neutrino oscillations", Physica Scripta **2005**, 57–64 (2004).

[63] I. Esteban, M. C. Gonzalez-Garcia, M. Maltoni, T. Schwetz, and A. Zhou, "The fate of hints: updated global analysis of three-flavor neutrino oscillations", Journal of High Energy Physics **2020**, 178, 178 (2020).

[64] P Sadowski, B Radics, Ananya, Y Yamazaki, and P Baldi, "Efficient antihydrogen detection in antimatter physics by deep learning", Journal of Physics Communications **1**, 025001 (2017).

[65] P. Sadowski and P. Baldi, "Deep learning in the natural sciences: applications to physics", in Braverman readings in machine learning (2017).

[66] D. Dwyer, M. Garcia-Sciveres, D. Gnani, C. Grace, S. Kohn, M. Kramer, A. Krieger, C. Lin, K. Luk, P. Madigan, C. Marshall, H. Steiner, and T. Stezelberger, "Larpix: demonstration of low-power 3d pixelated charge readout for liquid argon time projection chambers", Journal of Instrumentation **13**, P10007 (2018).

[67] J. Asaadi, M. Auger, A. Ereditato, D. Goeldi, R. Hänni, U. Kose, I. Kreslo, D. Lorca, M. Luethi, C. R. von Rohr, J. Sinclair, F. Stocker, C. Tognina, and M. Weber, "A pixelated charge readout for liquid argon time projection chambers", Journal of Instrumentation **13**, C02008 (2018).

[68] B. Abi et al., *Deep underground neutrino experiment (dune), far detector technical design report, volume ii: dune physics*, 2020.

[69] B. Abi et al., "Volume iii. dune far detector technical coordination", Journal of Instrumentation **15**, T08009 (2020).

[70] B. Abi et al., "Volume iv. the dune far detector single-phase technology", Journal of Instrumentation **15**, T08010 (2020).

[71] R. Acciarri et al., *Long-baseline neutrino facility (lbnf) and deep underground neutrino experiment (dune) conceptual design report volume 1: the lbnf and dune projects*, 2016.

[72] L. Paulucci and on behalf of DUNE collaboration, "The dune vertical drift photon detection system", Journal of Instrumentation **17**, C01067 (2022).

[73] J. Joshi and X. Qian, *Signal processing in the microboone lartpc*, 2015.

[74] D. Nygren and Y. Mei, *Q-pix: pixel-scale signal capture for kiloton liquid argon tpc detectors: time-to-charge waveform capture, local clocks, dynamic networks*, 2018.

[75] M. Rooks, S. Abbaszadeh, J. Asaadi, M. Febbraro, R. W. Gladen, E. Gramellini, K. Hellier, F. M. Blaszczyk, and A. D. McDonald, *Development of a novel, windowless, amorphous selenium based photodetector for use in liquid noble detectors*, 2022.

[76] S. Kubota et al., "Enhanced low-energy supernova burst detection in large liquid argon time projection chambers enabled by q-pix", Phys. Rev. D **106**, 032011 (2022).

[77] S. Agostinelli et al., "Geant4—a simulation toolkit", Nuclear Instruments and Methods in Physics Research Section A: Accelerators, Spectrometers, Detectors and Associated Equipment **506**, 250–303 (2003).

[78]Lattice, *Ice40 ultraplus family data sheet*, lattice ice40up fpga data sheet, Lattice Semiconductor (https://www.latticesemi.com/-/media/LatticeSemi/Documents/DataSheets/iCE/iCE40-UltraPlus-Family-Data-Sheet.ashx).

[79]Y. Li, T. Tsang, C. Thorn, X. Qian, M. Diwan, J. Joshi, S. Kettell, W. Morse, T. Rao, J. Stewart, W. Tang, and B. Viren, "Measurement of longitudinal electron diffusion in liquid argon", Nuclear Instruments and Methods in Physics Research Section A: Accelerators, Spectrometers, Detectors and Associated Equipment **816**, 160–170 (2016).

[80]A. Galindo-Tellez, K. Keefe, E. Adamek, E. Brubaker, B. Crow, R. Dorrill, A. Druetzler, C. J. Felix, N. Kaneshige, J. G. Learned, J. J. Manfredi, K. Nishimura, B. Pinto Souza, D. Schoen, and M. Sweany, "Design and calibration of an optically segmented single volume scatter camera for neutron imaging", Journal of Instrumentation **16**, P04013, P04013 (2021).

A p p e n d i x   A

SVSC OS1

the work in this subsection details the work and results of [80].

A p p e n d i x   B

SVSC OS2

Put OS2 work here